Improving the preclinical and clinical success rates of LMW drugs depends on radical revisions to the status quo scientific foundations of medicinal chemistry: a case study on COVID M^{pro} inhibition

Robert A. Pearlstein*[1†], Hongbin Wan[1†], Sarah Williams[2]

[1]Novartis Institutes for BioMedical Research, 181 Massachusetts Ave, Cambridge, MA 02139

[2]Novartis Institutes for BioMedical Research, 5959 Horton Street, Suite 900, Emeryville, CA 94608

[†]These authors contributed equally to this work

*Corresponding author: Robert A. Pearlstein, Ph.D.

Phone: +1 617-871-7293

Email: robert.pearlstein@novartis.com

Abstract

The poor preclinical and clinical success rates of low molecular weight compounds is partially attributable to the inherent trial-and-error nature of pharmaceutical research, which is limited largely to retrospective data-driven, rather than prospective prediction-driven workflows stemming from: 1) inadequate scientific understanding of structure-activity, structure-property, and structure-free energy relationships; 2) disconnects between empirical models derived from in vitro equilibrium data (e.g., Hill and Michaelis-Menten models) vis-à-vis the native non-equilibrium cellular setting (where the pertinent metrics consist of rates, rather than equilibrium state distributions); and 3) inadequate understanding of the non-linear dynamic (NLD) basis of cellular function and disease. We argue that the limit of understanding of cellular function/dysfunction and pharmacology based on empirical principles (observation/inference) has been reached, and that further progress depends on understanding these phenomena at the first principles theoretical level. Toward that end, we are developing and applying a theory on the mechanisms by which: 1) cellular functions are conveyed by dynamic multi-molecular/-ionic (multi-flux) systems operating in the NLD regime; 2) cellular dysfunction results from molecular dysfunction; 3) molecular structure and function are powered by covalent/non-covalent forms of free energy; and 4) cellular dysfunction is corrected pharmacologically. Our theory represents a radical departure from the status quo empirical science and reduction to practice thereof, replacing: 1) the interatomic contact model of structure-free energy and structure-property relationships with a solvation free energy model; 2) equilibrium drug-target occupancy models with dynamic models accounting for time-dependent drug and target/off-target binding site buildup and decay; and 3) linear models of molecular structure-function and multi-molecular/-ionic systems conveying cellular function and dysfunction with NLD models that more realistically capture the emergent behaviors of such systems. Here, we apply our theory to COVID M^{pro} inhibition and overview its implications for a holistic, in vivo relevant approach to drug design.

Introduction

Drug discovery is analogous to navigating a multi-dimensional maze with multiple entrances (i.e., targets + chemical starting points), few exits (i.e., approved drugs), and many blind alleys in between. Successful navigation depends on finding one or more paths to a safe therapeutic index (TI) in humans, the overall odds of which (P_d) are determined by the following sets of conditional probabilities:

$$P_d = P(CTI \mid T) \cdot P(CTI \mid CC, L, H) \cdot P(CC \mid L, H) \cdot P(L \mid H); \text{ and}$$
$$P(CTI \mid CC, L, H) \cdot P(CTI \mid T) \qquad [1]$$

where T is a biomolecular target on the path to efficacy, CTI is a clinical candidate for which a safe TI is achieved in clinical testing, CC are clinical candidates on the path to the CTI, L is a lead series on the path to the CC, H are hits on the path to L, and $P(x_n \mid x_{n+1}, \ldots, x_{n+m})$ are the conditional probabilities of success at each step of the process (e.g., CC depends on L, which depends on H). P_d is low by all accounts,[1] which is partially attributable to heavy reliance on trial-and-error synthesis and testing workflows guided by poorly predictive experimental and computational models for target and off-target potency (structure-activity/structure-free energy), solubility, permeability, and pharmacokinetic/ADMET (absorption, distribution, metabolism, elimination, and toxicity) properties relevant to the human setting. **Scaling the number of successful outcomes at the current P_d depends on scaling the number of attempts, whereas improving the underlying $P(x_n \mid x_{n+1}, \ldots, x_{n+m})$ depends on improving the predictiveness of the aforementioned models.** All scientific disciplines are broadly comprised of empirical and theoretical/first principles branches. Empirical science is based on observations of "what", "where", and "when" (the parts, systems, and behaviors thereof), the "how" and "why" (the mechanisms), which are inferred anecdotally or from statistical correlations with other observations that in some cases lead to empirical "laws". For example, Newton <u>inferred</u> that gravity is an invisible <u>attractive</u> force (F) between masses m_1 and m_2 that is proportional to their magnitude and inversely proportional to their distance apart ($F = G \cdot m_1 \cdot m_2/r^2$). Theoretical science is based on deductive/logical reasoning that extends beyond observation. For example, Einstein <u>deduced</u> that space is a substance that is perturbed unfavorably by masses and partially relaxes by <u>pushing</u> them together. Empirical science depends heavily on technology to extend the powers of observation, as well as for curating and analyzing the resulting data. Theoretical science is based on, and inspired by, empirical data combined with out-of-the-box human thinking. The major scientific theories, including special/general relativity, quantum mechanics, the standard model of particle physics, and number theory originated from physics and math. Conversely, chemistry is a largely empirical science (with the exception of quantum chemistry) that revolves around empirical models that are incorrect, inadequate, or right for the wrong reasons when:

1) Fit to noisy or under-sampled data (noting that weak signals can be extracted from low signal-to-noise data using machine learning (ML) or artificial intelligence (AI) as long as the signals are present in the data).

2) Fit using descriptors/parameters that poorly explain the data, often resulting in overfitting (i.e., a disproportionate number of descriptors/parameters relative to the size of the dataset).

3) Fit to data measured in one context and extrapolated to another.

4) Focused on scalar rather than vector quantities needed to explain multi-dimensional phenomena.

Inferences and predictions based on empirical models are often poor for the aforementioned reasons, but may be correct in one or more contexts (e.g., Newton's empirical gravitational law predicts well except under conditions of extreme gravity, whereas general relativity predicts well except in black holes). Empirical science is best suited for observing "what", "where", and "when", whereas "how" and "why" are best explained via first principles deduction. Biology is rooted in empirical chemistry, and as such, suffers from many of the same limitations when it comes to explaining the "how" and "why" of cellular phenomena. In this work, we:

1) Revisit the "how" and "why" of cellular function conveyed by multi-molecular and multi-ionic systems, cellular dysfunction conveyed by dysfunctional molecules, and pharmacodynamics through the lens of a novel first principles theory called Biodynamics[2–6] that we have been developing, testing, and applying to a wide range of problems over the last several years, including COVID M^{pro} structure-function and inhibition,[5] cereblon structure-function,[7] GPCR structure-function,[8] voltage-gated ion channel structure-function,[8] hERG blockade[9,10] and cellular arrhythmia[6].

2) Revisit our previous work on COVID M^{pro}, focusing on the structure-binding free energy relationships of the inhibitors nirmatrelvir and an analog thereof (PF-00835231).

3) Connect the dots between molecular structure-function/dysfunction, drug-target/off-target binding, pharmacokinetics (PK), pharmacodynamics (PD), and non-covalent free energy within and between the atomic and systems levels, and examine the implications thereof for improving P_d based on in vivo relevant drug design.

Toward a first principles understanding of the "how" and "why" of living cells

Cells are comprised of molecular and ionic "moving parts" bound together into organized multi-molecular/ionic systems that rearrange non-randomly and non-linearly over time (commonly referred to as non-linear dynamic or "complex" systems).[11] In fact, nearly all natural systems comprised of three or more moving parts, ranging from subatomic particles to atoms, molecules, atmospheres, oceans, stars, solar systems, and the Universe itself behave non-linearly (noting that linear systems may be comprised of thousands or more moving parts). All non-linear dynamic (NLD) systems are powered by attractive and repulsive forms of energy that are counter-balanced within a Goldilocks zone in which both the bound state and rearrangeability are maintained over time (e.g., gravity vis-à-vis fusion in the case of stars, gravity vis-à-vis kinetic energy in the case of solar systems, and electromagnetic attraction vis-à-vis kinetic energy in the case of atoms and covalent bonds). Science, in general, revolves largely around observing, describing, explaining, and predicting the configurational states and behaviors of natural NLD systems (many of which are strange and seemingly magical). Such systems:

1) **"Synthesize/solve" their overall behaviors (commonly referred to as "emergence")**, which in all cases, exceed the sum of the behaviors of their constituent parts (where the behavior of each part depends on the behavior of the entire system, and the behavior of the entire system depends on the behaviors of the parts and their mutual interactions). As such, NLD behaviors can only be observed or simulated, but not predicted analytically (i.e., they are deterministically unpredictable).

2) **Exhibit chaotic behaviors at perturbation-induced tipping points** (e.g., cardiac arrhythmias caused by perturbation of the normal dynamic inward-outward ion current

balance; ice ages caused by perturbation of the normal dynamic atmospheric-oceanic-geothermal balance; implosions/explosions of stars caused by the loss of dynamic balance between gravity and fusion-driven thermal expansion).

3) **Respond to perturbations in a non-causal fashion**, where causes are effects and effects are causes.

4) **Are powered by non-equilibrium free energy flows** between high and low states (referred to as "sources" and "sinks", respectively), analogous to the flow of air from high to low pressure regions of the atmosphere. The molecular populations of cellular systems build and decay via synthesis (sources) and degradation (sinks), as do their non-covalently bound states, which are powered within a Goldilocks zone of favorable and unfavorable energy contributions consisting principally of thermal, covalent, and desolvation and resolvation gains and costs (described below).

Living cells comprise a unique class of natural NLD systems in that their moving parts consist exclusively of micro/nano/pico/femto quantities of diverse ions and low and high molecular weight (LMW and HMW) species operating on the microscopic length and time scales (subserving high density information storage and fast information processing), versus bulk quantities of molecules operating on the geologic length and time scales (e.g., the atmosphere), and heavenly bodies operating on the cosmic length and time scales. Cells "solve" their behavior at each instant of time via a form of "physical math", commonly known as "analog computing", in which the hardware (molecules and ions) and software (the NLD state of the system) are one and the same. The normal and abnormal behaviors of macromolecular constituents and multi-molecular/multi-ionic systems conveying cellular functions cannot be understood or reliably predicted via empirical models based on equilibrium data measured on the isolated parts (equating to tacit linearization of such systems) or even intact cultured (typically, immortal) cell lines. Further progress toward this end depends on connecting the dots within and between target selection and clinical candidate generation (in vitro → native cellular) aimed at increasing P(CTI | T) and P(CTI | CC, L, H).

Improved predictions of biological behaviors and the effects of drugs thereon depends on first principles theoretical understanding of the cellular "playbook" shared by all natural NLD systems, including the means by which they are powered by covalent and non-covalent free energy forms in the native cellular setting (where non-covalent free energy exists solely in the form of barriers). We proposed that such barriers consist principally of molecular desolvation and resolvation costs,[5,7–10,12–16] which was inspired by the pioneering work of McKay and Kurtzman on the microscopic behaviors of solvating water.[3] Our work has led to novel insights about the general mechanisms by which:

1) Free energy is transduced into molecular structure and function, including the folding of HMW species and non-covalent binding between HMW-LMW and HMW-HMW species.

2) Cellular functions are conveyed by multi-molecular and multi-ionic systems operating in the non-equilibrium/NLD regime.

The reduction to practice of Biodynamics consists of first principles analyses and simulations of:

1) **Solvation free energy, which we postulate is the principal form of free energy powering non-covalent inter- and intramolecular rearrangements**,[5] versus interatomic contacts under the status quo paradigm (noting that improved P(CC | L, H) and P(L | H) depends heavily on the correct understanding of structure-free energy relationships).

Solvation free energy is qualitatively mirrored by the position-dependent occupancy of solvating water on the external surfaces of LMW molecules and the external and internal/buried surfaces of HMW molecules (noting that scalar solvation free energies cannot be predicted accurately via force-field-based methods, or practically via quantum chemical methods). The spatial distribution of solvation free energies across a given solute surface relative to bulk solvent (which may be external or internal in the case of folded HMW species) depends on the local H-bonding environment of each solvating water (the collective properties of which we refer to as the "solvation field"). Solvation fields residing at the binding interfaces of cognate partners, including drugs and their respective targets, are complementary to varying degrees (i.e., H-bond enriched to H-bond enriched and H-bond depleted to H-bond depleted). We refer to these regions as "solvophores" and "inverse solvophores" (borrowing from the pharmacophore-inverse pharmacophore concept) and the collection of solvophores and inverse solvophores across the entire endogenous biomolecular space as the "Solvome".[7] We postulated that k_{on} and k_{off} (as well as k_{in} and k_{out} in the case of intramolecular rearrangements) are proportional to the association/entry and dissociation/exit free energy barriers (denoted as $\Delta G^{\ddagger}_{association}$ and $\Delta G^{\ddagger}_{dissociaion}$ in the case of intermolecular rearrangements, and $\Delta G^{\ddagger}_{entry}$ and $\Delta G^{\ddagger}_{exit}$ in the case of intramolecular rearrangements) contributed principally by the desolvation and resolvation costs of the partners and intramolecular rearrangement interfaces (see below).[14] As such, non-covalent inter- and intramolecular rearrangements are governed by separate structure-association/entry and structure-dissociation/exit relationships. **Contrary to popular belief, solvation free energy is comprised of both enthalpic and entropic contributions**, as follows:[3]

   a) The H-bond enthalpy of liquid water per unit effective molecular volume (30 Å^3 per water) is by far the greatest among all liquid solvents and dissolved aqueous substances, to the extent that non-covalent solute structure and the dynamic properties thereof are powered principally by the minimization of water H-bond enthalpy at the maximum possible entropy.[3]

   b) Entropy losses relative to bulk solvent (taken as zero entropy) occur to varying degrees in solvating water in proportion to the degree of ordering required to minimize the water-water and water-solute H-bond free energy (commonly referred to as entropy-enthalpy compensation).

2) The normal and abnormal behaviors of mutant and WT proteins in the context of their native NLD cellular systems, versus in isolation under the status quo paradigm.[4,6] The resulting models can, in principle, be used to qualitatively predict efficacious drug-target combinations with improved P(CTI | T). NLD behaviors at both the atomic (e.g., multi-body intra-protein and protein-water interactions during protein folding and binding), and multi-molecular system levels that convey cellular functions are implicit to our theory.

3) Non-covalent binding under non-equilibrium conditions, in which binding sites build and decay over time (which we refer to as “binding dynamics”) versus the status quo static equilibrium paradigm. As such, cellular functions are governed by rates (i.e., the fastest fluxes), rather than the equilibrium distributions of the participating species.

The objective of lead optimization under the status quo paradigm consists of minimizing drug-target ΔG, IC_{50}, K_d, or K_i, while maintaining permeability, solubility, and other properties. However, the Biodynamics approach is aimed at achieving the Goldilocks zone of balanced drug solvation properties governing drug-target binding (minimal drug and target desolvation costs underlying $\Delta G^{\ddagger}_{association}$; maximal drug and target resolvation costs underlying $\Delta G^{\ddagger}_{dissociaion}$), membrane permeability (minimal drug and membrane desolvation costs; minimal drug and membrane resolvation costs needed to circumvent partitioning), and solubility/solvation free energy for the following reasons:

1) ΔG is defined only for non-equilibrium conditions, whereas $\Delta G^{\ddagger}_{association}$ and $\Delta G^{\ddagger}_{dissociation}$ are defined for equilibrium and non-equilibrium conditions.

2) **Structure is physically linked to the separate $\Delta G^{\ddagger}_{association}$ and $\Delta G^{\ddagger}_{dissociation}$ contributions (and $\Delta G^{\ddagger}_{entry}$ and $\Delta G^{\ddagger}_{exit}$ in the case of intramolecular rearrangements) rather than ΔG per se**, which is merely the difference between these quantities (just as taxes are linked to income and expenses rather than bank balances).

3) Achieving the minimum efficacious drug-target occupancy for dynamic binding sites (denoted as γ_{eff}) at the lowest possible free C_{max} (thereby reducing the risk of off-target binding, tox, adverse effects, and side effects that degrade P(CTI | CC, L, H)) depends on parity between k_{on} and the rate of binding site buildup, and k_{off} and the rate of binding site decay.[2]

Binding is thus governed by dynamic contributions analogous to a continuous dance between the partners and solvating water, in which:

1) The partners associate at their inherent on-rate (k_{on} · [free partner i](t) · [free partner j](t)), desolvating their H-bond enriched, bulk-like, and H-bond depleted solvation in the process.

2) The partners dissociate at their intrinsic off-rate (k_{off} · [partner i-partner j](t)), in which their external H-bond enriched and bulk-like surface positions and external (and in some cases internal) H-bond depleted surface positions are resolvated in the process.

3) Water exchanges to/from bulk solvent and solvation incur:
    a) Entropic gains and losses resulting respectively from water transfer to/from solvation to bulk solvent.
    b) Enthalpic losses due to desolvation of H-bond enriched positions (partially offset by drug-target H-bond enthalpic gains) and gains due to resolvation of H-bond enriched positions (partially offset by drug-target H-bond enthalpic losses).
    c) Enthalpic gains due to desolvation of H-bond depleted positions and losses from resolvation of H-bond depleted positions.

Materials and methods

We used molecular dynamics simulations and WATMD to predict the positions and qualitative magnitudes of H-bond enriched, depleted, and bulk-like solvation on the external and internal surfaces of COVID M^{pro} (previous work[5]) and the external surfaces of the M^{pro} inhibitors nirmatrelvir and PF-00835231 (current work). Since WATMD calculations are focused on water exchanges rather than solute rearrangements, we refer to these simulations as "solvation dynamics (SD) simulations" (noting that predicted solute rearrangements are highly unreliable due to the overestimation of interatomic contact energies and underestimation of solvation free energy by force-field-based methods). Our overall method is fully described in references 5, 7, and 10 and briefly summarized here:

1) Nirmatrelvir (PF-07321332)[17] and PF-00835231[18] were extracted from their crystallized M^{pro}-bound structures (PDB code = 7SI9[17] and 6XHM,[18] respectively).

2) The inhibitors were simulated in their fully restrained conformations using AMBER 20[19,20] PMEMD CUDA (GAFF and ff99sb force-fields) for 100 nanoseconds (ns) in a box of explicit TIP3P water molecules.

3) The fully unrestrained monomeric M^{pro} structure (PDB code = 2QCY[21]) was simulated in the same manner using AMBER 16.

4) The time-averaged hydrogen (H) and oxygen (O) occupancies within a stationary three-dimensional grid comprised of 1 Å^3 voxels in which each solute structure was embedded were calculated over the last 40,000 frames (10 ns) of the trajectory using WATMD V9[3,16,22] (noting that the solvation fully converges within 100 ns).

5) The high and low occupancy voxel data was normalized to the bulk-like solvating water (i.e., the mean of the distribution) on a solute-by-solute basis, so as to achieve self-consistency (WATMD calculations can be considered as first principles for this reason). The high occupancy voxels were then scaled to the largest voxel in the entire dataset.

6) The voxels were assigned to bulk-like, H-bond enriched, and H-bond depleted solvation states (noting that the results in all cases are distributed in a Gaussian fashion, the specific properties of which vary among solutes), as follows:

    a) **Bulk and bulk-like voxels** reside at the mean of the distribution, where the H and O positions in the same voxel are fully uncorrelated (corresponding to no orientational preference of the occupying water molecule).

   b) **H-bond depleted voxels** reside in the extreme left tail of the distribution (where $G_{bulk} < G_{solvation}$).

   c) **H-bond enriched voxels** reside in the extreme right tail of the distribution (where $G_{bulk} > G_{solvation}$).

7) Water occupancies are underestimated in voxels that are transiently occupied by mobile solute atoms that compete with water exchanges. This problem is circumvented as follows:

   a) LMW solutes are simulated with full restraints (ideally in their crystallized bound conformations).

   b) HMW solutes that undergo large rearrangements are simulated with light restraints (noting that water exchanges to/from tight spaces are slowed by restrained solute motions, resulting in artificially magnified voxel sizes).

   c) HMW solutes that undergo small, localized rearrangements (e.g., the β-hairpin in COVID M^{pro}) are simulated without restraints, and each of the mobile region(s) are separately aligned across all of the frames during the WATMD calculations (and are therefore stationary relative to the voxel grid).

8) Overlays between the structures and predicted voxel occupancy data were visualized using PyMol 2.0 (Schrodinger, LLC), with the occupied voxels denoted by spheres, the sizes of which are proportional to the predicted H and O occupancies, and the colors of which denote the preference for O (red), H (blue), and neither (white).

In our previous work, we studied the catalytic cycle and solvation properties of COVID M^{pro} vis-à-vis a set of published inhibitors based on the aforementioned principles.[5] We deduced that:

1) M^{pro} binds to substrates and inhibitors in its monomeric form.

2) The catalytic site is activated by substrate binding, followed by dimerization.

3) Turnover is followed by product dissociation, deactivation, and dimer dissociation.

In this work, we predict the solvation properties of two published M^{pro} inhibitors and compare the complementarity thereof to that of the catalytic pocket.

Results

In our previous work, we used WATMD calculations to characterize the inverse solvophore of monomeric COVID M^{pro} (PDB code = 2QCY) and its complementarity to the distribution of polar and non-polar groups on nirmatrelvir extracted from the dimeric M^{pro} complex (PDB code = 7SI9) and an analog thereof (PF-0083521) extracted from the dimeric M^{pro} complex (PDB code = 6XHM) (Figure 1) (noting that our LMW WATMD capability was unavailable at that time).

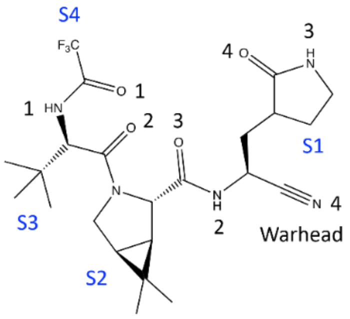

PF-07321332
SARS CoV2 M^{pro} K_i = 3.11 nM
Oral F = 50%

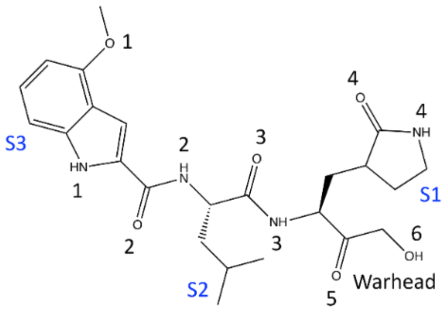

PF-00835231
SARS CoV2 M^{pro} K_i = 0.27 nM
Oral F = 1.4%

Figure 1. 2D structures and experimental data for the COVID M^{pro} inhibitors PF-07321332 (nirmatrelvir) and a crystallized analog thereof (PF-00835231).[18,23] The inhibitor side chains are labeled S1-S4. Oxygen and nitrogen atoms are numbered consecutively in the N- to C-terminal direction.

Both PF-07321332 and PF-0083521 react covalently with the catalytic cysteine of M^{pro}, resulting in accumulation of the covalent complex over time. The k_{on} of each inhibitor depends on the quality of mutual intermolecular H-bond replacements for H-bond enriched water expelled during association (noting that energetically conserved replacements need not be spatially conserved). The rate of occupancy accumulation depends on the slower of the on-rate or covalent reaction rate relative to the off-rate (noting that efficacy depends on equal or faster buildup of the inhibitor-bound state compared with the rate of M^{pro}-mediated polyprotein cleavage). It is reasonable to assume that the resolvation costs of the catalytic site and native substrates are calibrated for achieving $k_{-1} \lesssim k_{cat}$ (where k_{-1} is the substrate dissociation rate constant), whereas non-covalent inhibitors with smaller footprints that desolvate less H-bond depleted solvation than the native substrates likely exhibit $k_{off} > k_{-1}$. It is likewise reasonable to assume that the H-bond enriched solvation in the catalytic site is organized for optimal replacement by the maximum common solvophore among all of the endogenous M^{pro} substrates in the polyprotein (Figure 2). The H-bond enriched and depleted solvation in the catalytic site is highly complementary to that of PF-07321332 and PF-0083521 (described below). However, the actual k_{on}, the pre-reacted non-covalent k_{off}, and the post-reacted k_{off} cannot be quantitatively ascertained in the absence of measured kinetics data.

A

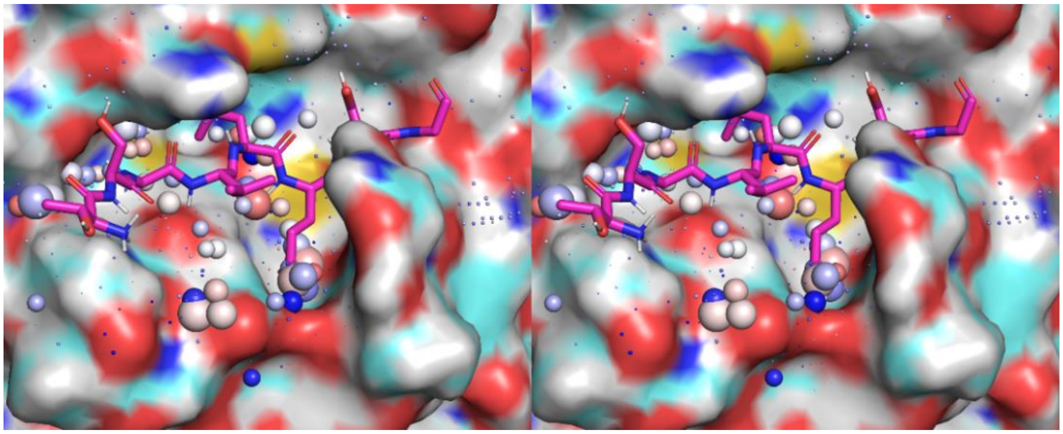

B

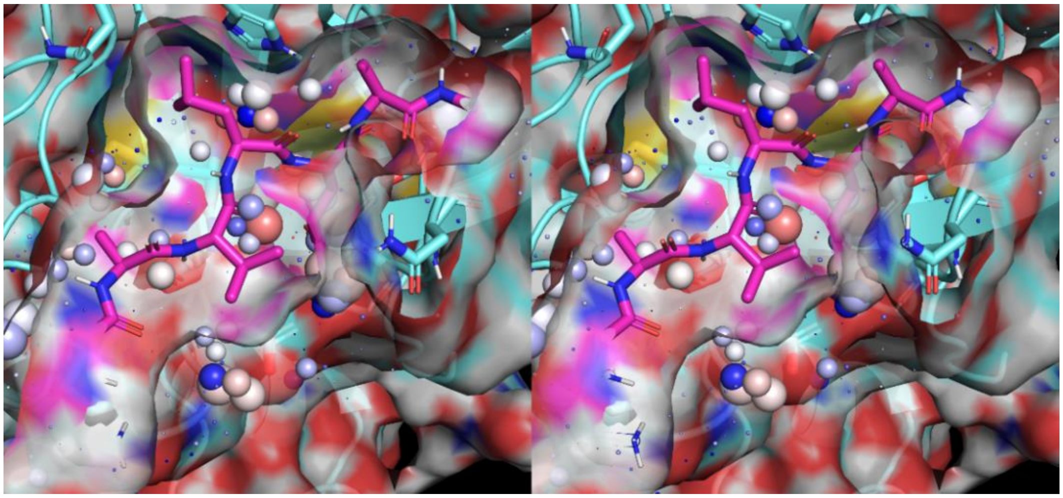

Figure 2. (A) Stereo view of the inverse solvophore of the apo monomeric mutant form of M^{pro} (PDB code = 2QCY) overlaid on an M^{pro} substrate extracted from PDB code = 2Q6G[5]. Low and high occupancy voxels are shown as color-coded spheres, as explained in Materials and methods (B) Same as A, except showing the solvent accessible surface of the substrate. All voxels contained within the substrate surface are expelled during association (noting that water is trapped within the northwestern region of the binding interface, and also exists in the southern region of the substrate-bound protein).

The solvophores of PF-0083521 (Figures 3A and 3B) and PF-07321332 (Figures 3C and 3D) share both similarities and differences in accordance with their unique shapes and polar/non-polar compositions and spatial distributions. Low occupancy/H-bond depleted voxels are distributed around the non-polar regions of both inhibitors, and high occupancy/H-bond enriched voxels are distributed as follows (referenced to the numbering shown in Figure 1):

> **PF-0083521**: Clusters of high occupancy voxels are concentrated around HN2 (ultra-high occupancy), HN3, HN4, and both of the oxygen lone pair positions of C=O2. High occupancy voxels are distributed in a chain-like fashion within a surface groove containing C=O2 and HN3 bounded by the warhead and S2 moieties. Low-cost desolvation of this inhibitor depends on the quality of H-bond replacements for each solvating water by appropriate M^{pro} H-bond partner(s). Low-cost desolvation of M^{pro} likewise depends on the quality of H-bond replacements for each solvating water in the catalytic site by appropriate inhibitor H-bond partner(s).

> **PF-07321332**: Clusters of high occupancy voxels are concentrated around HN1, HN2, and HN3 (with similar occupancy magnitudes at HN1 and HN2), together with both of the oxygen lone pair positions of C=O2. High occupancy voxels are distributed in a chain-like fashion within a surface groove containing HN2 (explained in reference 7). Desolvation of the high occupancy voxels at HN1 and HN2 is especially costly. Low-cost desolvation likewise depends on the aforementioned criteria.

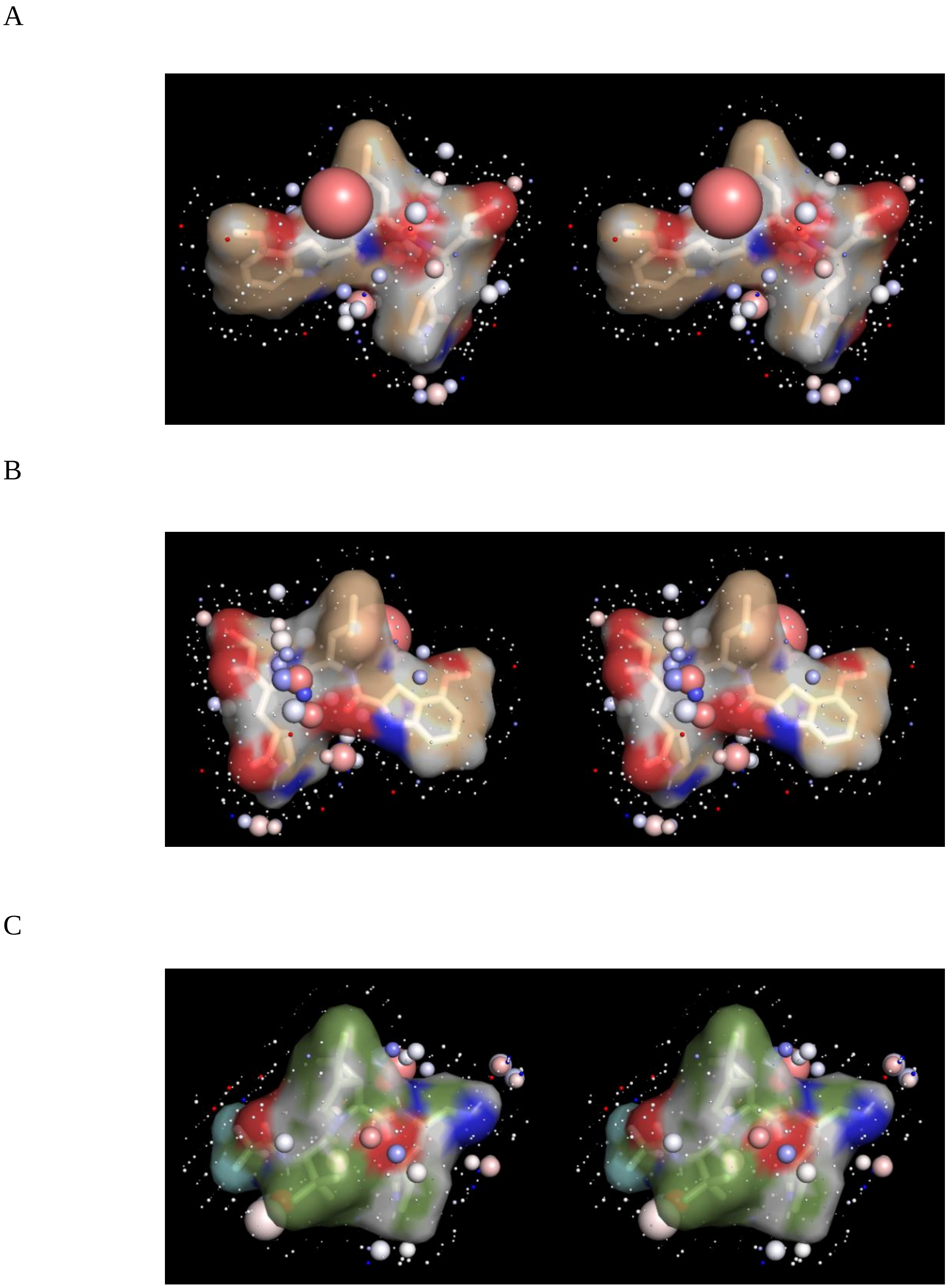
A
B
C

D

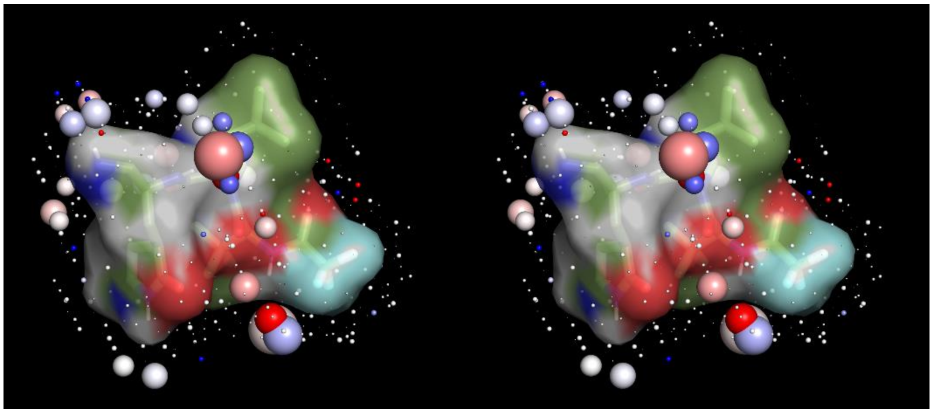

Figure 3. Stereo views of the structures and solvent accessible surfaces of the M^{pro} inhibitors PF-0083521 and PF-07321332 overlaid on their respective LMW solvophores calculated with WATMD (voxel annotations explained in Materials and methods). The inhibitor structures were extracted from the inhibitor bound M^{pro} crystal structures (see text), the warheads were manually restored to their pre-reacted states in preparation for the SD simulations, and the conformations were restrained in their crystallized conformations. (A) The solvent-facing side of PF-0083521 (tan sticks and transparent surface color-coded by atom type) with the reacted warhead on the right. (B) Same as A, except the pocket-facing side of PF-0083521 with the reacted warhead on the left. (C) The solvent-facing side of PF-07321332 (green sticks and transparent surface color-coded by atom type) with the reacted warhead on the right. (B) Same as C, except the pocket-facing side of PF-07321332 with the reacted warhead on the left.

The high potencies of both PF-0083521 and PF-07321332 are consistent with good overall packing within the M^{pro}-inhibitor interfaces (Figure 4) and high bidirectional complementarity between polar groups and high occupancy/H-bond enriched voxels of M^{pro} and PF-0083521 (Figure 5) and M^{pro} and PF-07321332 (Figure 6). However, mismatches between the CF_3 group of PF-07321332, high occupancy voxels in the P4 region, and suboptimal packing in the P2 region of M^{pro} (Figure 5A) may contribute to the ~10-fold lower potency of this inhibitor (which is offset by its substantially higher bioavailability (Figure 1)).

A

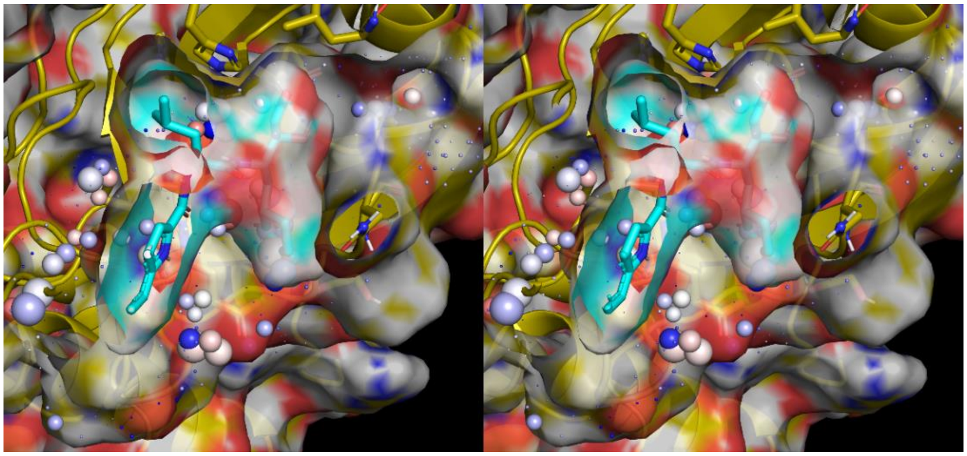

B

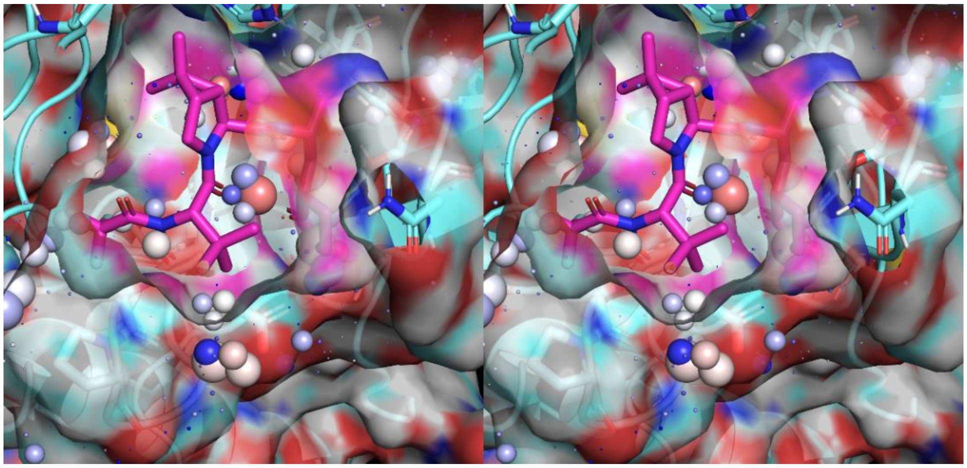

C

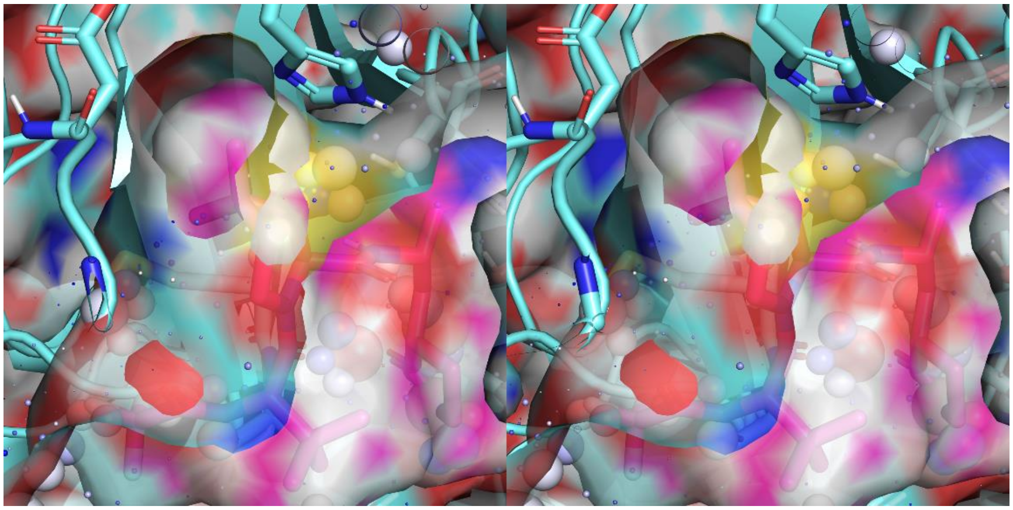

Figure 4. (A) Stereo view of the packing between apo monomeric M^{pro} (2QCY) and PF-07321332 (voxel annotations described in Materials and methods). All voxels contained within the substrate surface are expelled during association. (B) Same as A, except for PF-0083521 extracted from 6XHM. (C) Same as B, except showing the comparatively poor packing in the P2 pocket region occupied by trapped water.

A

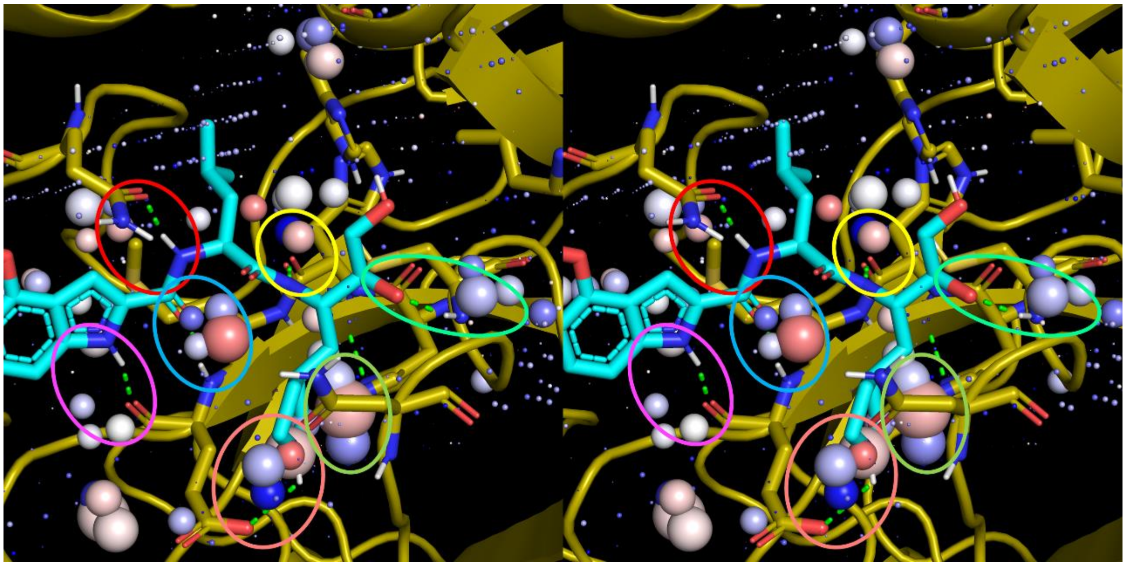

B

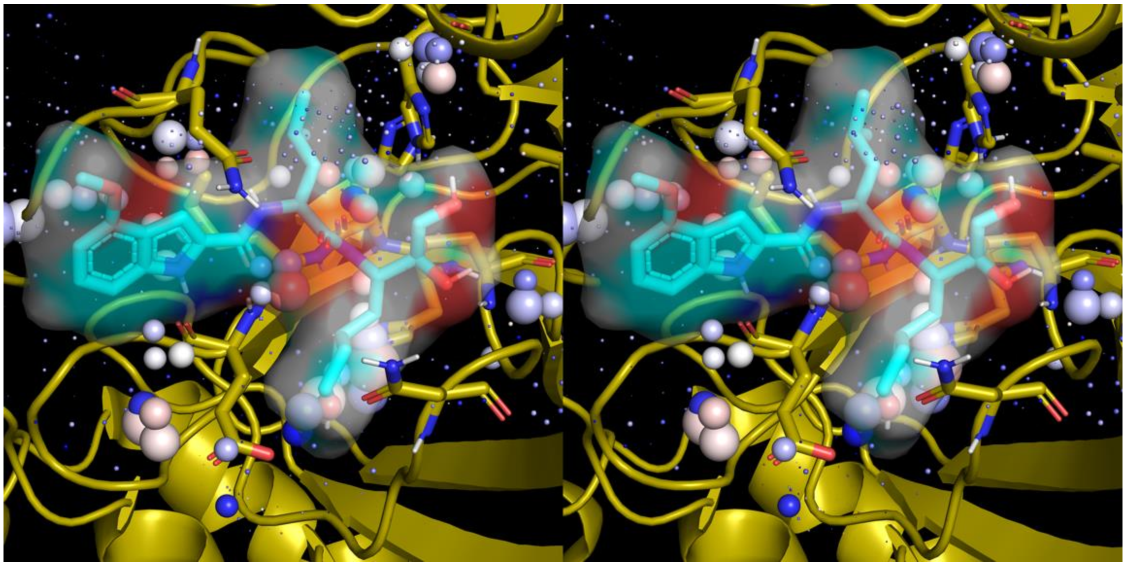

C

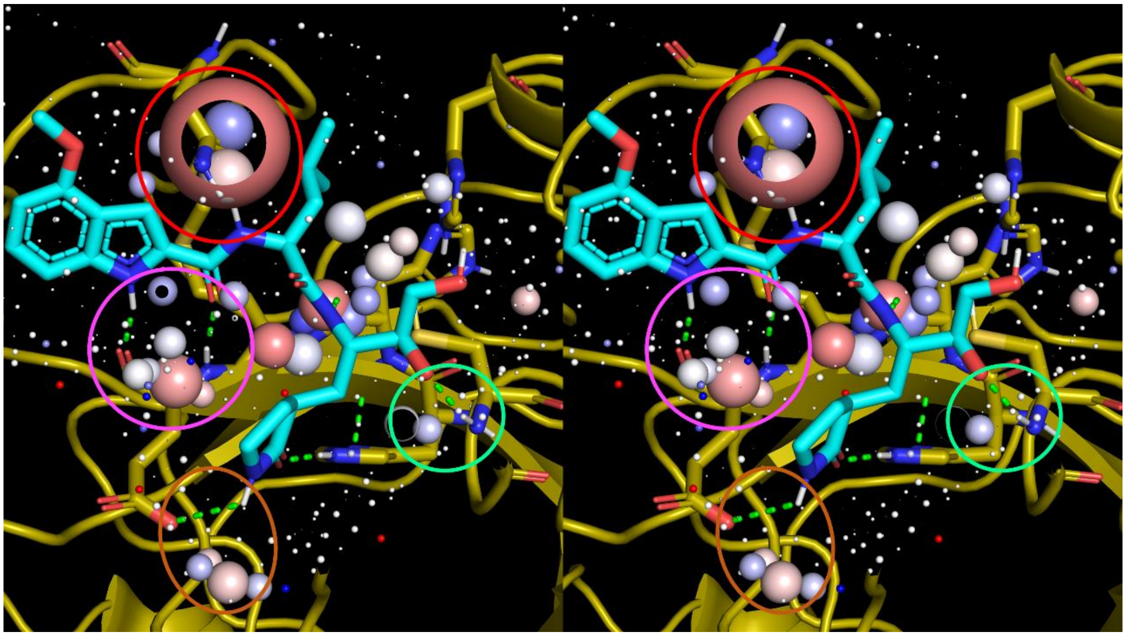

D

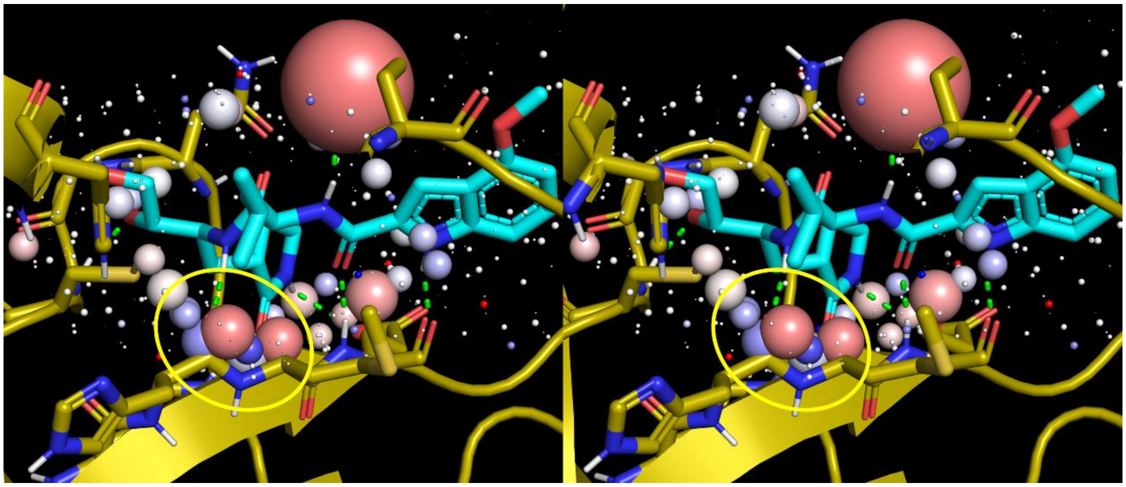

E

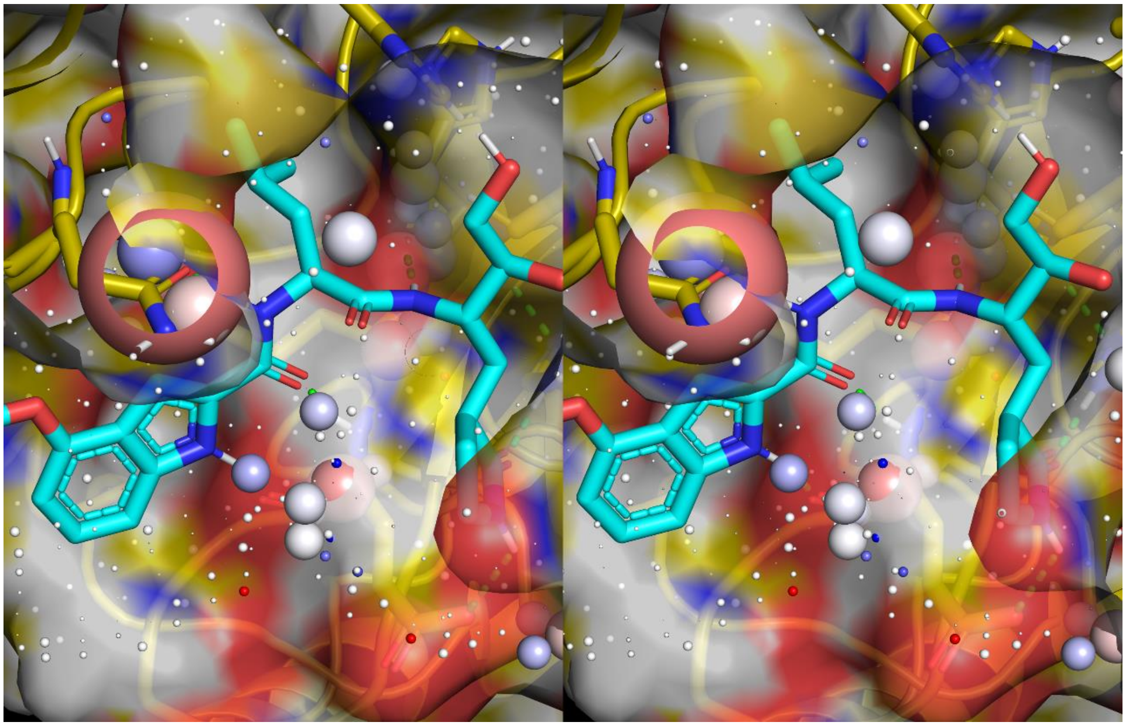

Figure 5. (A) Stereo view of PF-0083521 extracted from 6XHM overlaid on the inverse solvophore of apo monomeric M^{pro} (PDB code = 2QCY), showing protein-inhibitor H-bond replacements for the six high occupancy/H-bond enriched M^{pro} voxel clusters circled in magenta, orange, blue, green, lime green, and yellow (voxel annotations explained in Materials and methods). Protein-inhibitor water H-bond replacements are shown as green dotted lines (noting that the H-bond between His163 and S1 lactam oxygen is hidden by the voxels within the lime green circle). The H-bond between Gln189 and HN2 replaces the high occupancy inhibitor voxels shown in C. We postulate that viral resistance to PF-0083521 is likely achievable via mutation of Gln189 to amino acids that are incapable of desolvating the HN2 position of the inhibitor (noting that large voxels are fortuitously absent in PF-07321332). (B) Same as A, except showing the solvent accessible surface of PF-0083521. All M^{pro} voxels within the bounds of this surface are desolvated. (C) Front stereo view of apo monomeric M^{pro} overlaid on the solvophore of PF-0083521, showing the protein-inhibitor water H-bond replacements for the four high occupancy voxels circled in red and magenta. The protein-inhibitor H-bonds are shown as green dotted lines. The large voxel at HN2 is replaced by Gln189 (cutaway view). (D) Same as C, except viewed from the rear, showing the protein-inhibitor water H-bond replacements for the chain of high occupancy voxels proximal to HN3 (yellow circle). (E) Same as D, except showing the solvent accessible surface of M^{pro}. All the inhibitor voxels within the bounds of this surface are desolvated.

A

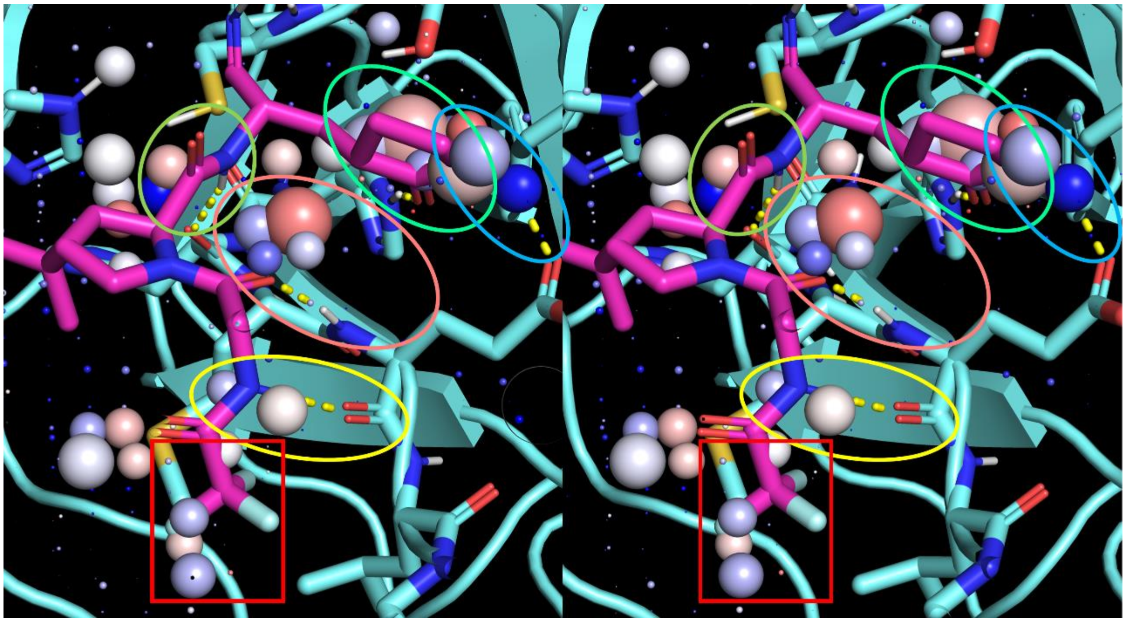

B

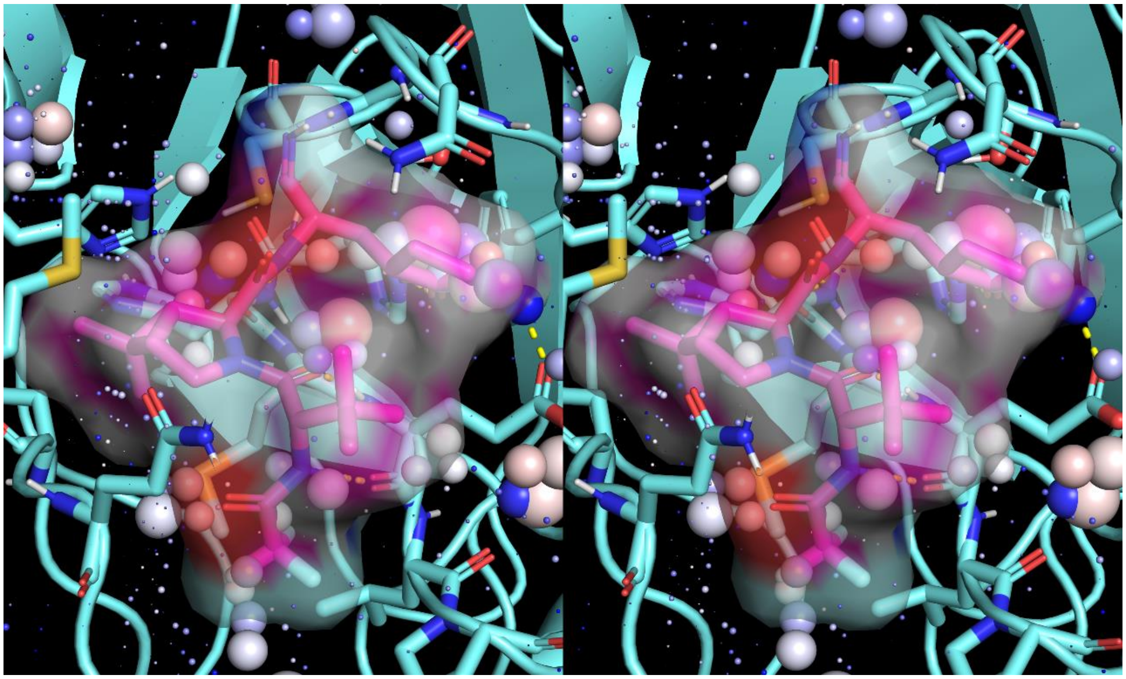

C

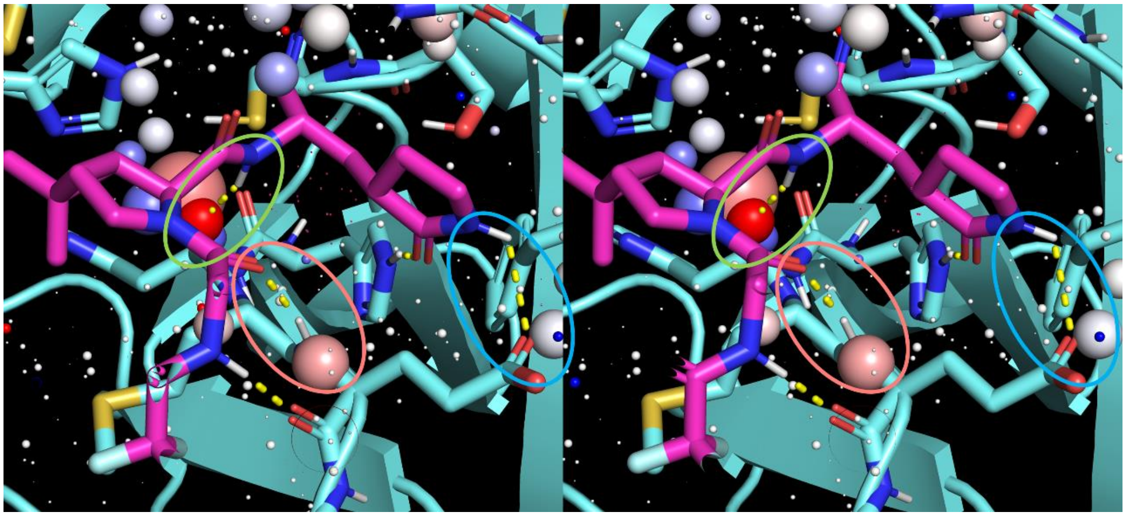

D

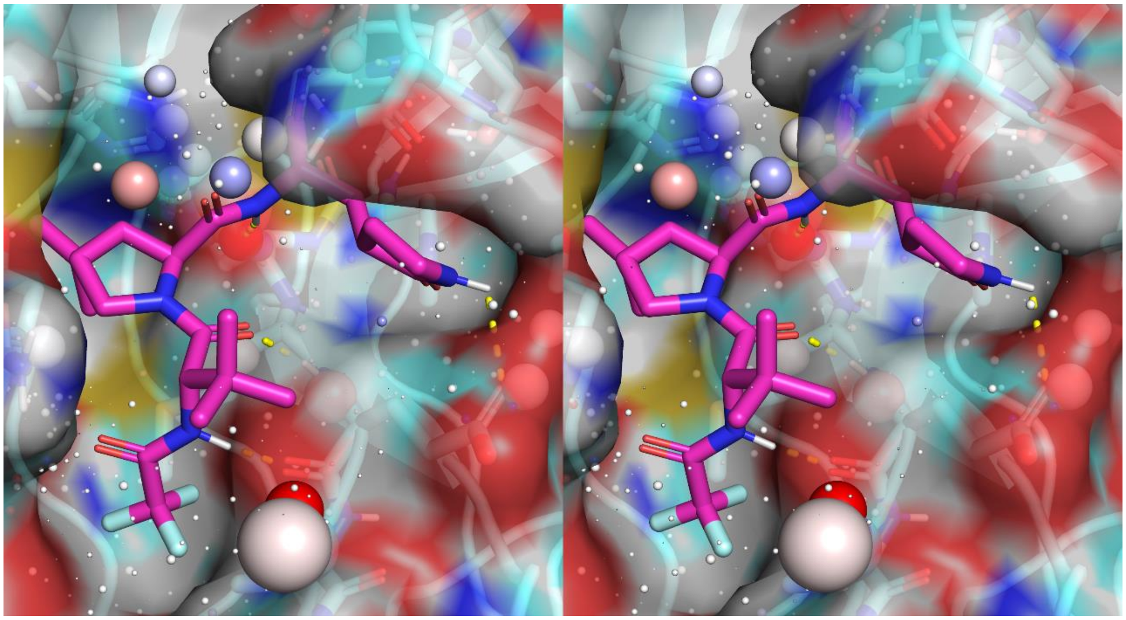

Figure 6. (A) Stereo view of PF-07321332 overlaid on the <u>inverse solvophore</u> of apo monomeric mutant M^{pro}, showing the protein-inhibitor H-bond replacements for the five high occupancy/H-bond enriched M^{pro} voxel clusters circled in, orange, blue, green, lime green, and yellow (voxel annotations explained in Materials and methods). Slowed k_{on} is expected due to the mismatch

bioRxiv preprint doi: https://doi.org/10.1101/2022.10.31.514572; this version posted November 2, 2022. The copyright holder for this preprint (which was not certified by peer review) is the author/funder. All rights reserved. No reuse allowed without permission.

between the inhibitor CF_3 group and the high occupancy voxel cluster enclosed in the red rectangle. The protein-inhibitor H-bond water replacements are shown as yellow dotted lines. (B) Same as A, except showing the solvent accessible surface of PF-07321332. All the M^{pro} voxels within the bounds of this surface are desolvated. (C) Stereo view of apo monomeric M^{pro} overlaid on the solvophore of PF-07321332, showing the protein-inhibitor water H-bond replacements for the three high occupancy voxels circled in orange, green, and blue. (D) Same as C, except showing the solvent accessible surface of M^{pro}. All the inhibitor voxels within the bounds of this surface are desolvated.

Discussion

In our previous work, we deduced the putative catalytic mechanism of COVID M^{pro} (which resembles that of caspase-2) and proposed a symbolic mathematical model based on equations 2 (see below).[5] In this work, we qualitatively deduced that nirmatrelvir and an analog thereof exhibit fast k_{on} and slow k_{off} to/from the M^{pro} catalytic site based on the high predicted complementarity between the inverse solvophore of M^{pro} and the inhibitor solvophores. In the following sections, we discuss the general implications of Biodynamics for in vivo relevant drug design.

The implications of non-equilibrium NLD behavior for medicinal chemistry, computational chemistry, and data science

In our previous work, we postulated that cellular function is predicated on the notion of "physical math" (commonly known as analog computing), the "physical equations" of which are comprised of temporospatial changes in the concentrations or number densities of molecular species and the covalent and non-covalent intra- and/or intermolecular states thereof (which we refer to as "fluxes").[4,7] Cellular functions (equating to emergent behaviors) are conveyed by specific sets of fluxes and static species (e.g., static CDK levels and dynamic cyclin levels) that are coupled together into systems via transient non-covalent binding and persistent enzyme-catalyzed covalent reactions (e.g., phosphorylation, ubiquitylation) (Figure 7A). **As mentioned above, the NLD behavior of such systems is holistic in that the behaviors of each flux (including drug pharmacokinetics (PK) and drug-target pharmacodynamics (PD)) depend on the behaviors of the system and vice versa, and as such cannot be properly studied piecemeal or at equilibrium**. Fluxes build and decay exponentially, and are therefore subject to runaway behavior (i.e., over- and under-shooting). We postulate that such behavior is circumvented via dynamic counterbalancing between flux-anti-flux pairs ("Yins" and "Yangs"),[3,4] in which Yang buildups are "phased" relative to their corresponding Yins by "clocks" (with the intervening steps in the pathway serving as "ticks") (Figure 7B). We further postulate that many cellular diseases result from over- or undershooting functional flux levels due to mutation-induced Yin-Yang imbalances.

A

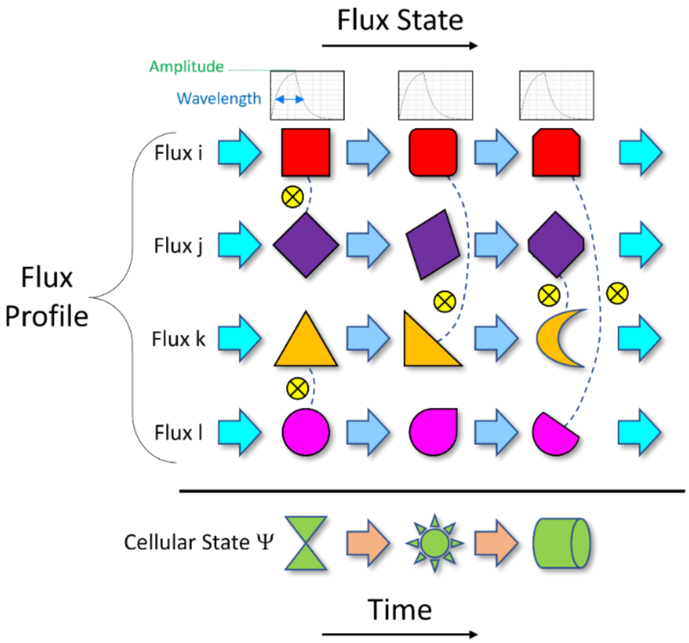

B

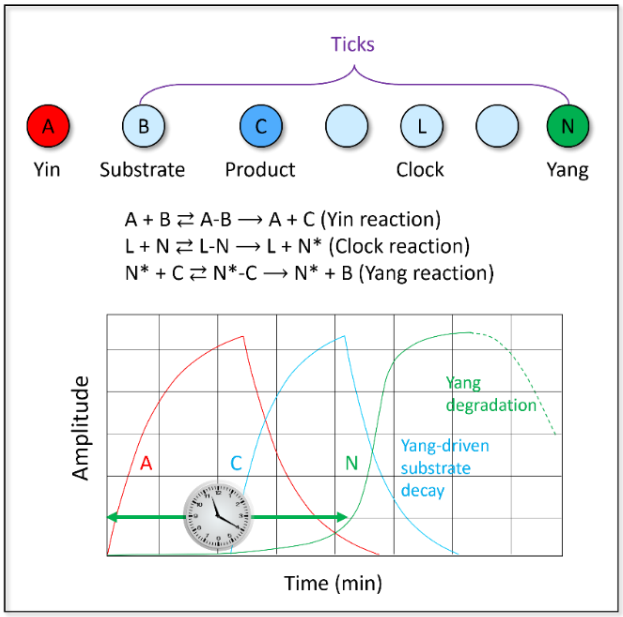

Figure 7. (A) Cellular functions are conveyed by systems comprised of multiple coupled molecular (and in some cases ionic) fluxes operating in the NLD regime. Each flux undergoes one or more non-covalent intra- and/or intermolecular and typically one or more covalent state transitions (e.g., phosphorylation, ubiquitylation). Fluxes build and decay exponentially in time via synthesis/degradation or covalent activation/deactivation. (B) Each flux ("Yin") is counterbalanced by an anti-flux ("Yang") so as to circumvent runaway exponential behavior. Yin-Yang phasing is governed by "clocks" that drive Yang buildups downstream of their respective Yins, with the intervening steps equating to "ticks".[4]

Non-covalent binding between fluxes i and j or flux i and static species j and enzymatic turnover are physical processes ("molecular differential equations" (MDEs)), the symbolic forms of which include the following:

$$d[\text{bound state}](t)/dt = \text{on-rate} - \text{off-rate} \qquad [2a]$$

$$\text{d[bound state](t)/dt} = k_{on} \cdot \text{[free flux i](t)} \cdot \text{[free flux j](t)} - k_{off} \cdot \text{[bound state](t)} \quad [2b]$$

$$\text{d[product](t)/dt} = k_1 \cdot \text{[free enzyme flux i](t)} \cdot \text{[free substrate flux j](t)} - k_{-1} \cdot \text{[enzyme-substrate](t)} - k_{cat} \cdot \text{[enzyme-substrate](t)} \quad [2c]$$

$$\text{d[bound state](t)/dt} = k_{on} \cdot \text{[free species i]} \cdot \text{[free flux j](t)} - k_{off} \cdot \text{[bound state](t)} \quad [2d]$$

where d[bound state](t)/dt denotes the difference between the on- and off-rates (equation 2a), equating to the rate of buildup or decay of the bound state of a cognate flux pair (equations 2b-2c) or a flux and its static cognate partner (equation 2d). d[bound state](t)/dt builds when on-rate > off-rate, decays when off-rate > on-rate, and remains constant when on-rate = off-rate (noting that the net decay rate is determined, in part, by re-binding, as reflected in the on-rate). Equation 2d contrasts with the equilibrium free concentration-occupancy relationship given by the Hill equation:

$$\text{bound fraction} = \text{[free species]}/(\text{[free species]} + K_d) \quad [3]$$

In the special case of drug-target binding:

$$\text{d[drug-target](t)/dt} = k_{on} \cdot \text{[free drug in the target compartment](t)} \cdot \text{[free target binding site](t)} - k_{off} \cdot \text{[drug-target](t)} \quad [4]$$

where d[free target binding site](t)/dt may vary from 0 (constant levels) to >> 0, case-by-case, and k_{on} determines the amount of free drug that can be "absorbed" by the target per unit time (where the binding site is overflowed by excess free drug).[2,4] In our previous work, we showed that:

1) Equation 4 converges to equation 3 when parity is maintained between k_{on} and k_{off} and the rates of binding site buildup (denoted k_i) and decay (denoted k_{-i}), respectively, which we refer to as "kinetically tuned binding" (Figure 8A).

2) Equation 4 is less than equation 3 and drug-target occupancy lags the dynamic free target concentration at all time points when k_{on} and k_{off} are mistuned to k_i and k_{-i}, respectively (in proportion to the degree of mistuning) (Figure 8B).

Caveat 1: Kinetic mistuning results in disconnects between the true versus expected minimum efficacious exposure in vivo, requiring dose escalation in the clinic to identify the true efficacious exposure (thereby eroding the safety margin, TI, and P(CTI | CC, L, H)).

A

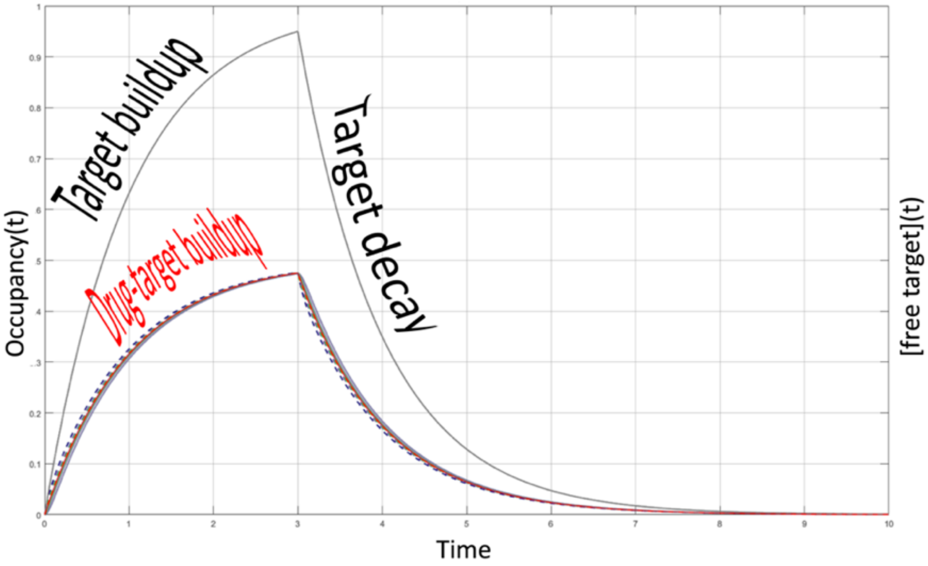

B

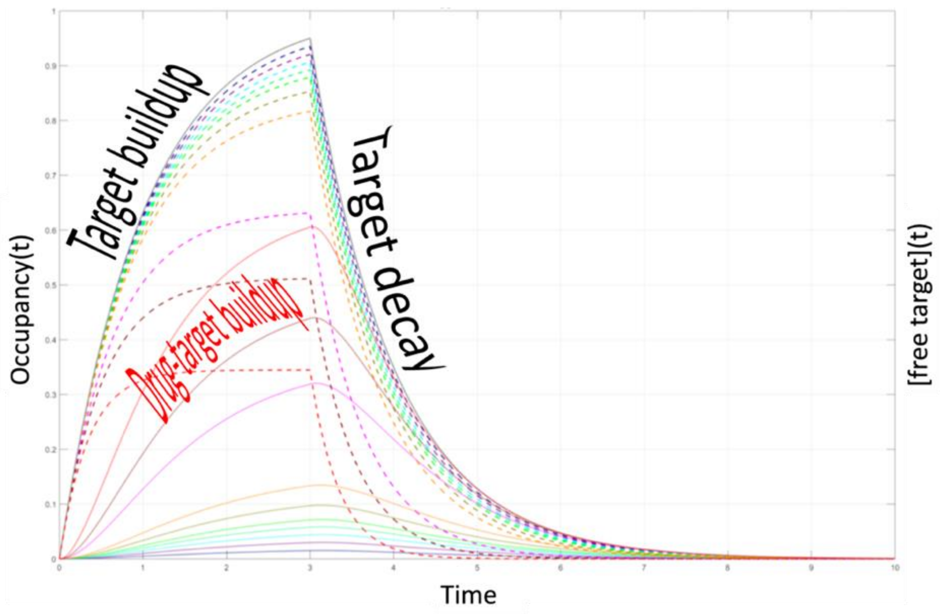

Figure 8. Hypothetical <u>simulated</u> target and drug-target buildup/decay curves for a given k_i, k_{-i}, k_{on}, and k_{off}.[2] The bound and free drug concentrations are represented by the solid and dotted tracings, respectively. (A) The kinetically tuned scenario in which k_{on} and k_{off} maintain parity with k_i and k_{-i}, respectively. Steady state occupancy = 50% of [free target](t) is achieved at all time points when [free drug] = K_d, and any given occupancy is achieved in multiples of K_d. (B) The kinetically mistuned scenario in which parity between k_{on} and k_i and/or k_{off} and k_{-i} is not achieved. In this scenario, non-steady state occupancy < steady state occupancy occurs at each time point, where [drug-target](t) buildup lags [free target](t) buildup. The expected minimum γ_{eff} in humans is underestimated in such cases, the true level of which is only achievable via dose escalation during clinical testing. **In the worst case scenario, binding is <u>mistuned to the therapeutic target</u> and <u>tuned to one or more off-targets</u> by happenstance**.

Cellular dysfunction (alteration of one or more “analog cellular programs”) putatively results from imbalances in one or more Yin-Yang pairs due to mutation-induced loss or gain of Yin, Yang, or clock molecular function (translating to over- or undershooting in the afflicted pathway(s)). Pharmacological intervention is putatively aimed at restoring the normal Yin-Yang balance (the pharmacodynamic response) by inhibiting or activating the dysfunctional target or other targets. Drug-target binding, in turn, depends on [free drug in target compartment](t) and [free target binding site](t), the former of which depends for oral drugs on the NLD balance between drug absorption (the source), clearance/metabolism (the permanent sink), and the fraction bound to a wide range of transient sinks, including off-target(s), membranes, plasma proteins, and lysosomes (Figure 9A), and the latter of which depends on the NLD balance between the target and overall system (noting that the same paradigm applies to off-target binding and the toxicodynamic responses thereto). Steady state free drug levels may be achieved, depending on the relative rates of the above processes vis-à-vis the dosing frequency.

The total free drug concentration in an in vivo system is given by:

$$\text{d[total free drug]/dt} = \text{rate of absorption} - \text{rate of association} + \text{rate of dissociation} - \text{rate of clearance} \quad [5]$$

where, for the sake of simplicity, the association and dissociation terms represent the aggregate of all endogenous species to which the drug binds. The direction of drug flow through the system is determined by the in-rates to the various compartments and on-rates to the various endogenous species within. The higher drug concentrations outside the central and peripheral compartments during the absorption phase drive inward flows to the peripheral compartments (i.e., where the in-rates exceed the out-rates) (Figures 9B and 9C), which reverses during the clearance phase (i.e., where the out-rates exceed the in-rates) (Figures 9B and 9D). Lags in this process are introduced by slow off-rates from one or more transient sinks (including drug-target in some cases).

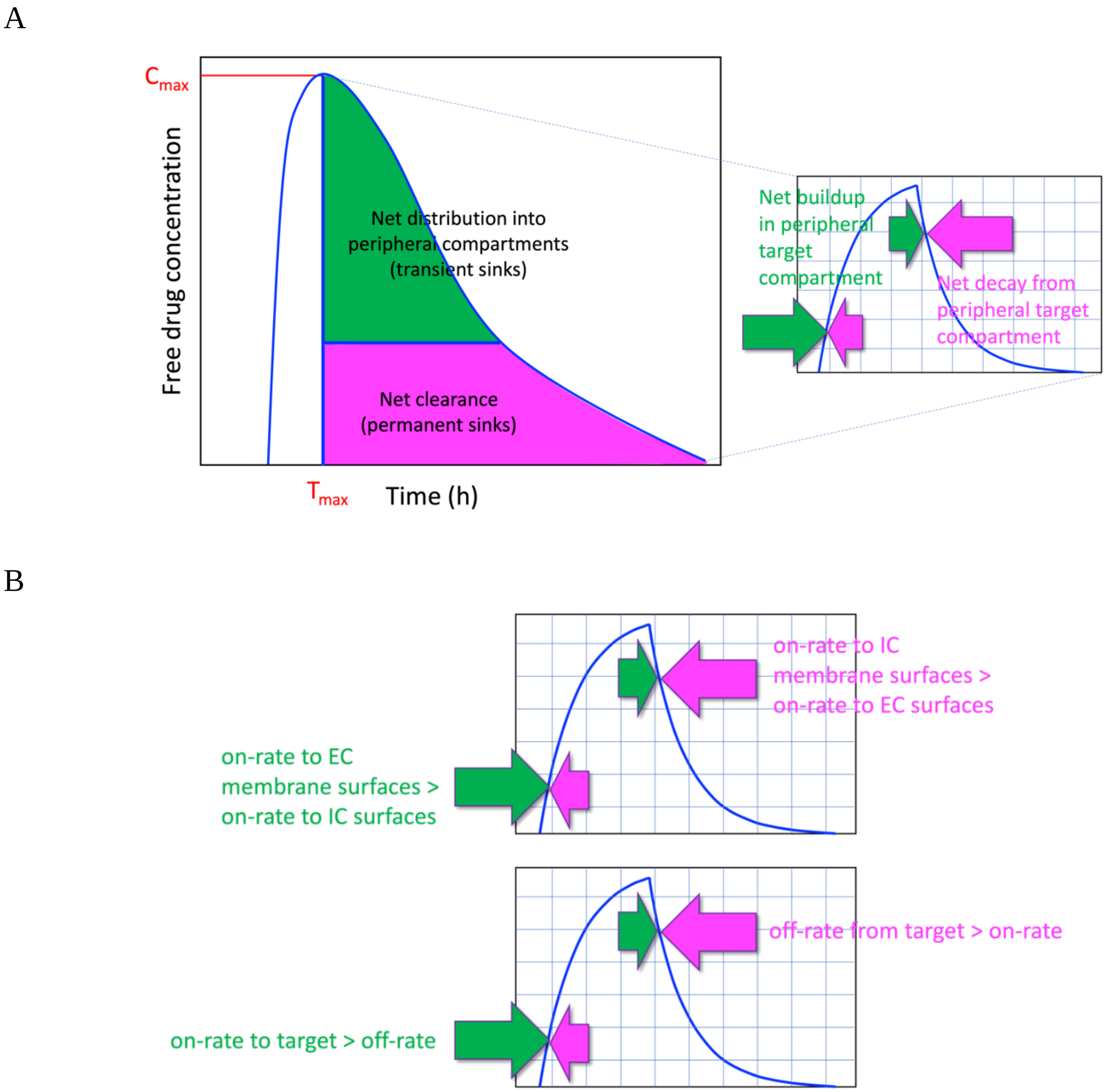

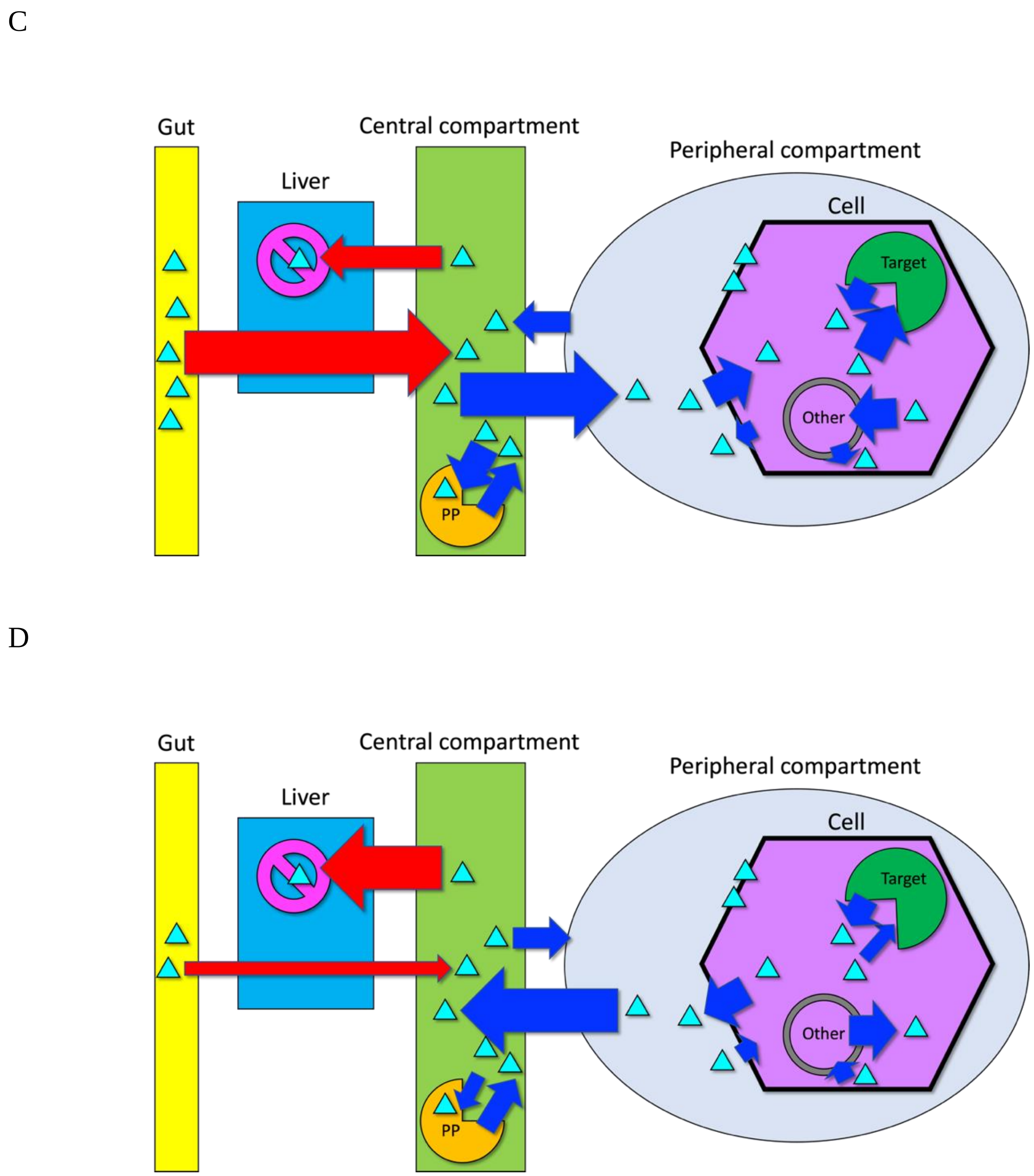

Figure 9. Drugs (cyan triangles) flow to and from the gut, central, and peripheral compartments along their concentration gradients in a highly non-linear source → sink fashion. (A) Hypothetical single oral dose PK curve, in which a drug is absorbed from the gut, followed by first-pass metabolism, distribution of the remaining fraction into the peripheral compartments, and binding to a wide range of intra- and extracellular species (including plasma proteins). All of these

processes operate concurrently, with faster absorption than distribution in the absorption (pre-C_{max}) phase, faster distribution than clearance in the distribution (early post-C_{max}) phase, and faster clearance than distribution in the clearance (late post-C_{max}) phase (resulting in reversal of drug flow back to the central compartment). (B) All source → sink processes (including transient distribution to/from peripheral compartments and binding, as well as permanent metabolic sinks) are bidirectional, with the fastest direction at a given time predominating (noting that lags in this process are introduced by slow off-rates from transient sinks). (C) The rates of drug entry into the central and peripheral compartments (red and blue arrows, respectively) are governed by the in-rate/out-rate balance to/from each compartment, where in-rate exceeds out-rate during the absorption phase. The fraction of drug bound to the various endogenous species residing within each compartment builds when the partner-specific on-rate exceeds the off-rate. (D) The rates of drug exit from the central and peripheral compartments (red and blue arrows, respectively) are governed by the out-rate/in-rate balance to/from each compartment, where the out-rate exceeds the in-rate during the clearance phase. The fraction of drug bound to its various endogenous partners decays when the partner-specific off-rate exceeds the on-rate.

The total free drug concentration in the central compartment, representing the fraction of total drug available for distribution, binding, and clearance, is given by:

$$\text{d[total free drug in central]/dt} = \text{rate of absorption} - \text{rate of plasma protein association} + \text{rate of plasma protein dissociation} - \text{rate of distribution} - \text{rate of clearance} \qquad [6]$$

noting that the extremely high plasma protein (PP) concentration (~500-700 μM^{24}) results in fast drug-PP on-rates:

$$\text{d[drug-PP]/dt} = k_{on} \cdot \text{[free drug in central](t)} \cdot (700\text{e-}6 - \text{[bound PP](t)}) - k_{off} \cdot \text{[drug-PP](t)} \qquad [7]$$

The free drug concentration in the extra-cellular compartment is given by:

$$\text{d[free extracellular drug]/dt} \approx \text{d[free drug in central]/dt} \qquad [8]$$

The free drug concentration in the intra-cellular target compartment is given by:

d[free drug in target compartment] = rate of inward permeation – rate of association + rate of dissociation – rate of outward permeation [9]

where the rate of inward permeation depends on [free extracellular drug](t), together with the rates of membrane entry and exit, and the rate of outward permeation depends on [free drug in target compartment](t), together with the rates of membrane entry and exit (<u>noting that slow membrane exit in either direction results in membrane accumulation/partitioning</u>).

The optimal PK-PD and PK-TD scenarios may now be described as follows (under the tacit assumption that PD is governed directly by the time-dependent drug-bound target fraction, and TD is governed directly by the time-dependent drug-bound fraction of the most toxic off-target):

1) Kinetically tuned <u>drug-target</u> binding, resulting in the minimum γ_{eff} at the lowest possible free C_{max}.

2) Kinetically mistuned <u>drug-off-target</u> binding, resulting in minimum off-target occupancy at the therapeutic free C_{max}.

3) Slow drug-PP k_{on}/fast k_{off}, such that [drug-PP](t) << rate of drug distribution.

4) [total free drug](t) > rate of clearance.

5) Clearance of the drug-target complex (-[drug-target](t)) < the rate needed to achieve the minimum γ_{eff}.

6) $n \cdot K_d$ < [free drug in target compartment](t), where $n \cdot K_d$ is the minimum efficacious exposure in the kinetically tuned binding scenario (e.g., $19 \cdot K_d$ → 95% drug-target occupancy). [free drug in target compartment](t) necessarily overshoots and decays back to the minimum efficacious exposure during the dosing interval (Figure 10A). Inter-dose troughs in [drug-target](t) result when [free drug in target compartment](t) decays to << $n \cdot K_d$.

7) Dosing interval/quantity is commensurate with conditions 3-5.

8) [total free drug](t) < upper safe limit (allowing for dose escalation due to overdose or drug-drug-interactions (DDIs)) (Figure 10B).

A

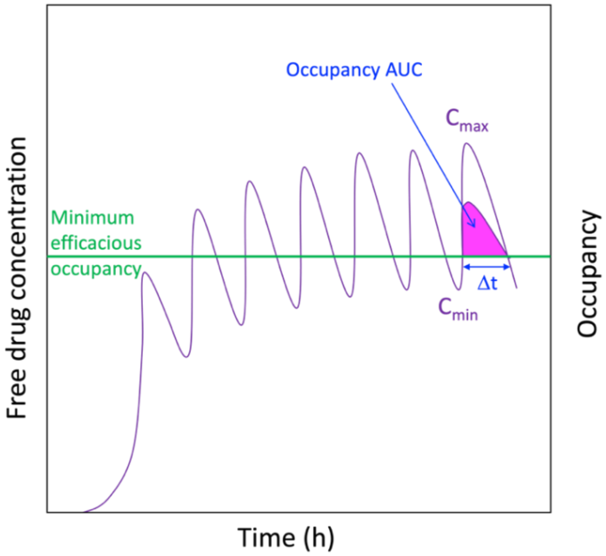

B

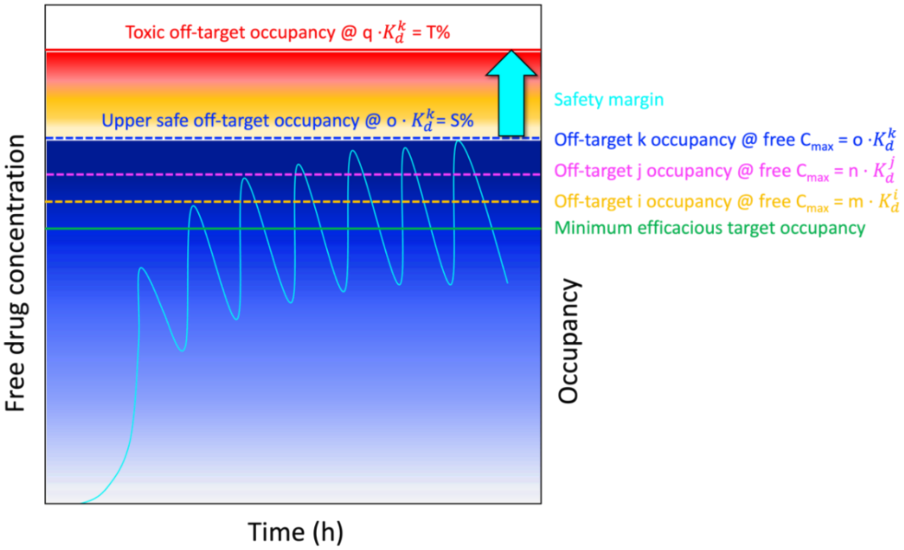

Figure 10. (A) Hypothetical multi-dose plasma PK curve, in which the free drug exposure builds to and overshoots the minimum γ_{eff} (topping out at the C_{max}), followed by decay to the sub-efficacious level (bottoming out at the C_{min}). The duration of action per dose (Δt) is governed by the degree to which the minimum γ_{eff} is overshot (represented by the area under the occupancy curve (AUC)). The minimum γ_{eff} is achieved at the lowest possible free C_{max} in cases of kinetically tuned binding. (B) Occupancy of a set of hypothetical off-targets i, j, and k as a function of the free plasma drug concentration ranging from the minimum efficacious exposure to the free C_{max}, where the K_d^x are the off-target binding constants (assuming the worst-case scenario of kinetically tuned off-target binding), n $\cdot$ K_d^x = C_{max} in multiples of K_d^x, and m $\cdot$ K_d^k = the toxic free drug concentration for off-target k in multiples of K_d^k.

The mutual effects of drugs on in vivo systems (i.e., PD) and in vivo systems on drugs (i.e., PK) is well appreciated in pharmaceutical science. The need for tight integration in PK-PD models (perhaps more than is commonly recognized) follows from the overtly NLD relationship among the underlying behaviors shown in Figure 9. Nevertheless, PK, potency, and efficacy are routinely characterized separately and later reassembled into PK-PD models, representing tacit linearization of these highly non-linear contributions. Equilibrium relationships between free drug concentration and occupancy are widely assumed in such models (equation 3), despite the known time dependence of the total drug concentration and possible time dependence of the targeted binding site concentration (in which case, kinetically mistuned drug-target binding resulting in reduced P(CC | L, H) and P(CTI | CC, L, H) is conceivable) (Figure 11). This practice may result in drug failures when the minimum efficacious equilibrium occupancy in vitro exceeds the minimum steady state γ_{eff} in vivo. Furthermore, lead optimization is hampered by poor understanding of structure-ADME, structure-target binding, and structure-off-target binding relationships that may likewise contribute drug failures.

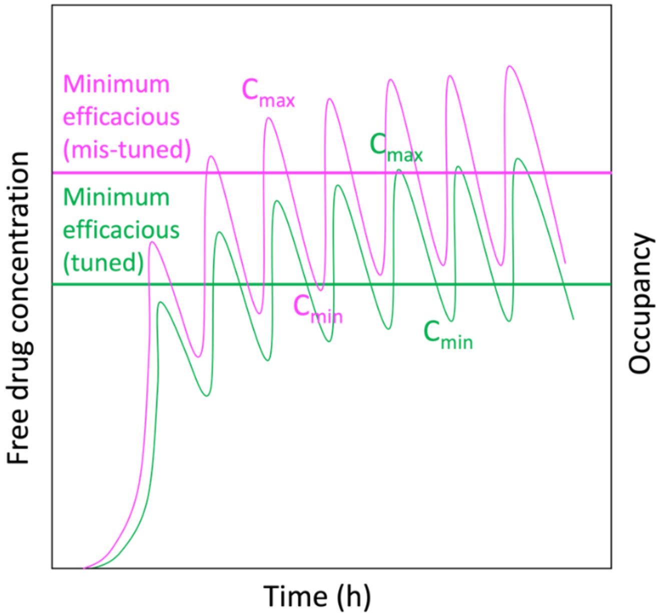

Figure 11. Kinetically mistuned drug-target binding results in a higher-than-expected minimum efficacious drug exposure in the target compartment under in vivo compared with in vitro conditions (in proportion to the gap between the rate of drug or target/binding site buildup and k_{on}), necessitating higher in vivo drug exposures to achieve the minimum γ_{eff}.[2]

The implications of the proposed solvation free energy model for medicinal chemistry, computational chemistry, and data science

Binding sites are classically viewed as molecular surfaces capable of forming complementary interatomic contacts with cognate partners, and non-covalent intra- and intermolecular free energies are widely assumed to originate principally from interatomic contacts partitioned into van der Waals, electrostatic, H-bond, π-π, π-cation, hydrophobic, hydrophilic, and lipophilic contributions (the basis of force-fields, docking scoring functions, and molecular descriptors used in a wide variety of empirical/QSAR models). This hypothesis is predicated on the assumption that free energy contributions are largely the same in the gas and solid phases as under aqueous conditions. **However, interatomic contact free energy contributions are far weaker than water-water and water-solute H-bonds under aqueous conditions** based on the following considerations:

1) The steep distance dependence of van der Waals and electrostatic enthalpy ($1/r^6$ and $1/r^2$, respectively), together with screening of electrostatic interactions by intervening water (reflected in the large dielectric constant of water), resulting in near zero enthalpic contributions at distances greater than the Debye length (how complementary contacts co-localize therefore becomes a chicken-egg problem).

2) The magnitude of van der Waals enthalpy summed over numerous contacts in LMW and HMW molecules is negligible relative to the H-bond enthalpy of liquid water.

3) Intra- and inter-solute H-bond and electrostatic enthalpy gains are offset to varying degrees by the high desolvation costs of polar and charged partners (a zero sum game at best).

4) π-π, π-cation, and halogen bonds are far weaker than water H-bonds, and under aqueous conditions, may be confused with the effects of cationic groups that enrich the H-bond enthalpy of their solvating water, versus aromatic rings and halogen groups that deplete it (noting that although halogens are highly electronegative, they do not share their electrons). Furthermore, enthalpic gains from π-cation contacts are likewise offset by the high cation desolvation cost.

5) The existence of hydrophobic (polar-non-polar), hydrophilic (polar-polar), and lipophilic (i.e., non-polar-non-polar) free energy contributions is strongly questioned by the lower enthalpies of water-methane compared with methane-methane interactions (which are significantly higher than that of water-water interactions) calculated using *ab initio* quantum mechanics.[3]

Conversely, water H-bond enthalpy is extremely large and water is highly sensitive to H-bond losses and gains in the presence of solutes, as follows:[3–5,7,14,22,25]

1) The non-polar regions of LMW and HMW solutes are solvated by high energy H-bond depleted water (relative to bulk solvent), the amount, magnitude, and spatial distribution of which are determined by the chemical structures and monomer sequences of LMW and HMW solutes, respectively.

2) H-bond depleted solvation is maximally present in the initial dissolved state at t = 0 and is partially or fully expelled to bulk solvent over time via intra- and intermolecular rearrangements (binding, folding) to or toward the equilibrium distribution at fixed and variable concentrations, respectively (Figure 12).

3) Residual H-bond depleted solvation that cannot be auto-desolvated in cis is invariably present to one degree or another in post-rearranged solute states, as follows:

    a) At non-polar regions of external surfaces, including binding sites and rearrangement interfaces.

    b) In the case of HMW solutes, within internal sub-surface cavities from which exchanges with bulk solvent are either slowed/impeded or abolished in the absence of surface openings.

4) Further intra- and/or intermolecular rearrangements initiated by perturbations are powered principally by the desolvation of residual H-bond depleted solvation (e.g., the introduction of a binding partner; change in membrane potential in the case of ion channels).[5,7,8]

5) Allosteric/remote effects are powered by the indirect concerted desolvation of internal solvation during binding partner association. Induced-fit effects are powered by the indirect concerted desolvation of internal and/or external H-bond depleted solvation located proximal to the binding interface.

6) k_{on} (the intermolecular association rate constant) and k_{in} (the intramolecular entry rate constant) are largely proportional to the mutual desolvation costs of the binding partners and rearrangement interface, respectively.[14] Desolvation costs, in turn, are proportional to

the H-bond free energy of H-bond enriched solvating water (denoted as G_{solv}) expelled from the inter- or intramolecular interface relative to bulk solvent (denoted as G_{bulk}), where $G_{bulk} - G_{solv} > 0$. The lower the G_{solv} of this water, the higher the desolvation cost.

7) Intra- and intermolecular rearrangements (including the opening of so-called cryptic pockets) leading to the de novo generation of H-bond depleted solvation (relative to the original state) are slowed in proportion to the magnitude of the solvation free energy loss (i.e., the association or entry barrier is increased by such solvation).

8) k_{off} (the intermolecular dissociation rate constant) and k_{out} (the rate of exit from a given intramolecular state) are proportional to the mutual resolvation costs of the binding partners and rearrangement interface, respectively.[14] Resolvation costs, in turn, are proportional to the H-bond free energy (relative to bulk solvent) of solvating water returning to H-bond depleted positions of the interface, where $G_{solv} - G_{bulk} > 0$. The higher the G_{solv} of this water, the higher the resolvation cost.

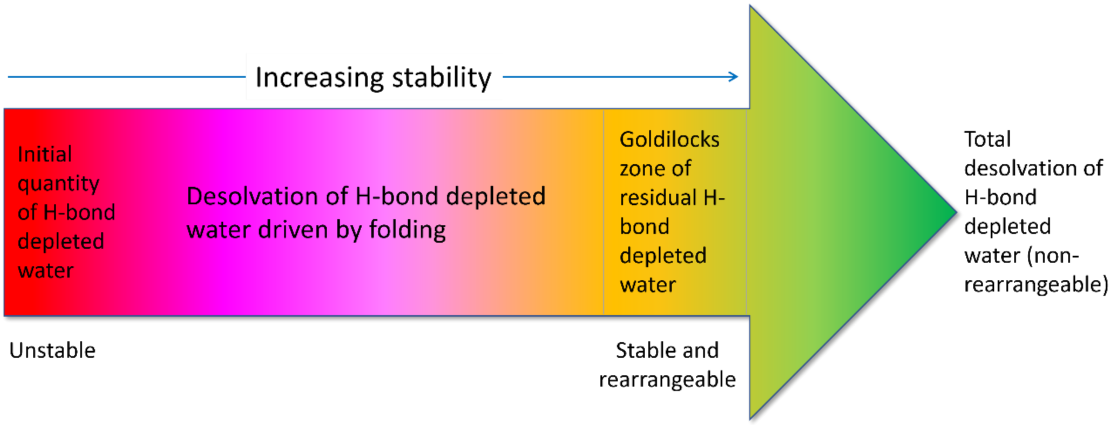

Figure 12. The introduction of HMW and LMW solutes to aqueous conditions (at t = 0) results in the generation of H-bond depleted surface solvation, the amount, magnitude, and distribution of which mirrors the non-polar surface composition. The minimum free energy states correspond to those in which the H-bond depleted solvation has been maximally auto-desolvated via intramolecular rearrangement/folding and/or H-bond enriched solvation has been gained in the rearranged state. However, total auto-desolvation of such solvation results in non-rearrangeability of the populated states.

The total non-covalent binding free energy can be derived as follows:

$$\Delta G_{\text{binding}} = \Delta G_{\text{interatomic solute contacts}} + (\Delta G_{\text{solute H-bond}} + \Delta G_{\text{desolvation}}) \qquad [10]$$

where $\Delta G_{\text{binding}}$ is the total free energy gain, $\Delta G_{\text{interatomic solute contacts}}$ is the interatomic contact free energy contribution, $\Delta G_{\text{desolvation}}$ is the water transfer free energy contribution, and $\Delta G_{\text{solute H-bond}}$ is the intra- or inter-solute H-bond free energy contribution. $\Delta G_{\text{interatomic solute contacts}}$ can be neglected to a first approximation, since $(\Delta G_{\text{solute H-bond}} + \Delta G_{\text{desolvation}}) >> \Delta G_{\text{interatomic solute contacts}}$:[3]

$$\Delta G_{\text{binding}} \cong \Delta G_{\text{solute H-bond}} + \Delta G_{\text{desolvation}} \qquad [11a]$$

$$\Delta G_{\text{binding}} \cong (\Delta G_{\text{solute H-bond}} + \Delta G_{\text{H-bond enriched desolvation}}) + \Delta G_{\text{H-bond depleted desolvation}} \qquad [11b]$$

where:

a) $\Delta G_{\text{interatomic solute contacts}}$ and $\Delta G_{\text{solute H-bond}}$ are always < 0.

b) $\Delta G_{\text{H-bond enriched desolvation}}$ is always > 0.

c) $\Delta G_{\text{solute H-bond}} + \Delta G_{\text{H-bond enriched desolvation}} \rightarrow 0$ as $\Delta G_{\text{solute H-bond}} \rightarrow \Delta G_{\text{H-bond enriched desolvation}}$.

d) $\Delta G_{binding} \rightarrow \Delta G_{H\text{-bond depleted desolvation}}$ (given perfect replacement of the H-bonds of desolvated H-bond enriched solvation).

Caveat 2: Interpretation of structure-activity relationships (the currency of medicinal chemistry) in terms of interatomic contact free energy contributions, the prediction of non-covalent free energy and structure-free energy relationships using force-field based approaches (e.g., molecular dynamics, free energy perturbation, conformational searching, energy minimization), and data modeling approaches (e.g., quantitative structure-activity relationship (QSAR) analysis, docking/scoring, pharmacophore analysis) are subject to grossly overestimated solute and grossly underestimated solvation contributions.

Equation 11b can be expressed as:

$$\Delta G_{binding} \cong \Delta G^{\ddagger}_{association} - \Delta G^{\ddagger}_{dissociation} \qquad [12]$$

where $\Delta G^{\ddagger}_{association}$ and $\Delta G^{\ddagger}_{dissociation}$ are the free energy barriers for entry and exit to/from an intermolecular state, respectively. Structure kinetics relationships can therefore be explained on the following basis (contrary to the classical structure-free energy interpretation):

1) The non-covalent entry free energy barrier magnitude equates to the net desolvation cost, consisting of the H-bond free energy lost in transferring H-bond enriched solvation to bulk solvent, offset by the free energy gained via intra- or inter-solute H-bond formation (typically > 0 and rarely < 0). As such, the populated non-covalent states are those entered the fastest, rather than those stabilized by intra- or inter-solute H-bonds and electrostatic contacts (as is widely assumed). **The most frequently visited states are those in which the lowest desolvation cost of H-bond enriched solvation (denoted as "gatekeeper**

solvation") is incurred during entry. A simple rule of thumb is that H-bonds observed in folded HMW species and complexes reflect the allowed positions of polar groups during folding or binding (i.e., where H-bond enriched solvation existed prior to folding or binding), whereas non-polar contacts reflect H-bond depleted positions that were desolvated during folding or binding.

2) The magnitude of the exit free energy barrier equates to the total <u>resolvation</u> cost <u>at H-bond depleted positions</u> incurred during decay of a given non-covalent intra- or intermolecular state. Non-covalent states are kinetically stabilized principally by this contribution, which may be augmented by π-stacking interactions <u>in fully dehydrated environments</u>. As such, **the most persistent states are those whose resolvation costs incurred at H-bond depleted solvation positions in the exited/dissociated state are the highest (denoted as "sticky solvation")**. Such solvation necessarily resides within a Goldilocks zone in which:

   a) Anti-solubilizing and destabilizing effects are balanced against low energy gatekeeper solvation.

   b) Non-specific intra- and intermolecular rearrangements that expel H-bond depleted solvation are minimized.

   c) Rate-determining steps (lags) due to slow off-rates of endogenous species are minimized.

3) Non-covalent states build and decay over time, wherein buildup exceeds decay in the net buildup phase (i.e., on-rate is increasing relative to off-rate) and decay exceeds buildup in the net decay phase (i.e., on-rate is slowing relative to off-rate) (Figure 9B, bottom).

Overview of Biodynamics-guided drug design

Improving P_d depends on a first principles approach to drug design, in which solubility, permeability, drug-target binding kinetics, and drug-off-target binding kinetics are addressed holistically according to the predicted distributions of H-bond enriched and depleted solvation of hit and lead compounds, target and off-target binding sites, and membrane surfaces (Figure 13) (ultimately aimed at "reverse-engineering" predicted inverse solvophores into LMW compounds capable of achieving optimal PK-PD relationships in humans). All such behaviors are considered in terms of their individual (i.e., $\Delta G^{\ddagger}_{association}$ and $\Delta G^{\ddagger}_{dissociation}$), rather than aggregated free energy (i.e., ΔG) contributions, consisting principally of the desolvation and resolvation costs incurred during rearrangements (where higher desolvation costs equate to lower solvation free energy and proportionately higher solubility at the expense of higher maximum $\Delta G^{\ddagger}_{association}$).

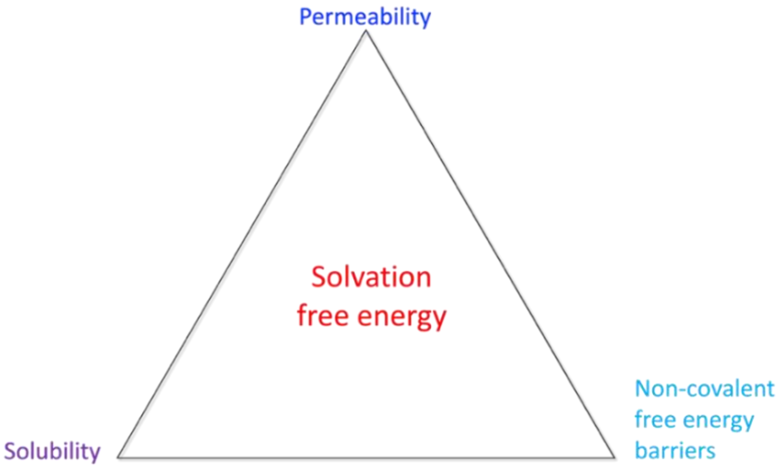

Figure 13. Solubility, permeability, and non-covalent intra- and intermolecular free energy barriers are governed principally by solvation free energy contributed by water-solute and water-water H-bond free energy contributions, which are spatially distributed over the solvent accessible surfaces of solutes. Of particular interest are regions of H-bond enriched and depleted solvation (relative to

bulk solvent) versus energetically neutral bulk-like solvation. Solubility (excluding dissolution) is a complex function of the relative proportions, magnitudes, and spatial distributions of H-bond enriched and depleted solvation at polar and non-polar solute surfaces, respectively (enhanced by the former and diminished by the latter). Solvation free energy, in turn, depends on the local H-bonding environment at each solute surface position (governed by local chemical composition and surface shape/curvature[7]). $\Delta G^{\ddagger}_{entry}$ and $\Delta G^{\ddagger}_{association}$ are proportional to the total desolvation cost of H-bond enriched solvation during entry or association, respectively, and $\Delta G^{\ddagger}_{exit}$ and $\Delta G^{\ddagger}_{dissociation}$ are proportional to the total resolvation cost at H-bond depleted positions during exit or dissociation. **The maximum $\Delta G^{\ddagger}_{entry}$ or $\Delta G^{\ddagger}_{association}$ increases with increasing solubility and total desolvation cost (replacing the H-bonds of H-bond enriched solvation needed to speed k_{on} becomes increasingly challenging), and the maximum $\Delta G^{\ddagger}_{exit}$ $\Delta G^{\ddagger}_{dissociation}$ increases with decreasing solubility and total resolvation cost.** Permeability is governed by $\Delta G^{\ddagger}_{entry}$ and $\Delta G^{\ddagger}_{exit}$ to/from phospholipid membranes, respectively. The skewed distribution of H-bond enriched and depleted solvation of amphipathic (phospholipid-like) solutes promotes membrane partitioning rather than permeation. The Lipinski Rule of 5 (reflecting the polar/non-polar composition)[26] equates to the Goldilocks zone of H-bond enriched and depleted solvation governing optimal solubility, target binding, and permeability.

According to our theory, the minimum free energy conformational states of LMW species are those tipped toward excess H-bond enriched versus H-bond depleted solvation (particularly trapped or impeded internal H-bond depleted solvation). The most populated sterically accessible conformational states of a given species under non-equilibrium conditions are those whose rates of entry (k^{i}_{in}) are fastest, and rates of exit (k^{i}_{out}) are slowest, versus those corresponding to free energy minima at equilibrium. The fastest k_{in}^{i}s are those exhibiting the lowest desolvation costs (i.e., in which H-bond enriched solvation is replaced by intra-solute H-bonds during entry or in which such solvation is altogether absent). The slowest k_{out}^{i}s are those exhibiting the highest resolvation costs (i.e., those in which large amounts of H-bond depleted solvation are expelled during entry). The actual conformational distributions of LMW species in solution may be considerably wider than those suggested by force-field-based calculations in which favorable enthalpic contributions are overestimated and entropic gains realized over wider distributions are underestimated. The preferred conformations are likely those in which the overall solvation free energy and electronic energy in the case of unsaturated or covalently rearrangeable moieties (e.g., tautomers) is minimized, as follows:

1) Extended conformations of highly polar compounds in which the polar groups are maximally solvated.

2) Conformations in which the H-bonds of H-bond enriched solvating water have been optimally replaced by intramolecular H-bonds (the rates of formation of which depend on the quality of the replacements vis-à-vis the desolvated H-bond enriched water). Such conformations are transient.

3) Folded conformations of larger solutes, in which H-bond depleted solvation has been maximally desolvated. The persistence of such conformations is proportional to the resolvation cost incurred upon exiting.

Desolvation and resolvation costs are likewise considered in terms of their individual (vectorial) contributions at the internal and external surface positions of HMW solutes and the external surface positions of LMW solutes, versus conventional measured and calculated scalar quantities under the status quo paradigm (e.g., binding constants, binding free energy, solubility, permeability, logP) (Figure 14).

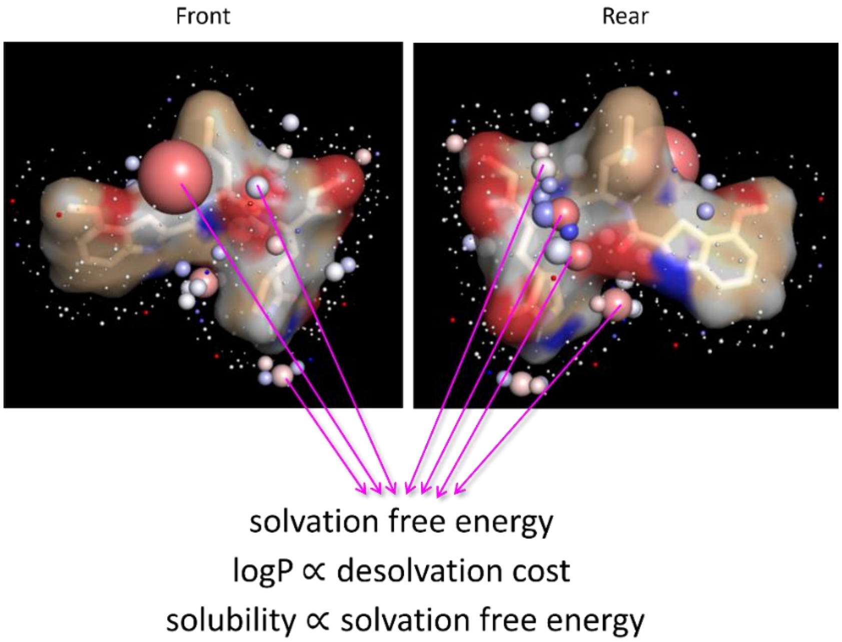

Figure 14. The high occupancy voxels of the M^{pro} inhibitor PF-0083521 calculated using WATMD (see below) overlaid on the solvent accessible surface of the compound (showing the front and rear faces). The total desolvation cost (i.e., -(the total solvation free energy)), which is proportional to logP is proportional to the qualitative sum of the desolvation costs at each voxel position, which in turn, are proportional to the voxel radii (reflecting the time-averaged water occupancy relative to bulk solvent). LogP serves as a benchmark of the overall voxel radii-desolvation free energy relationship (noting that the spatial distribution of the individual contributions to the desolvation and solvation free energies is more useful than scalar logP values for the purpose of drug design).

Furthermore, target sequence → drug approaches are precluded by the inherently non-linear nature of drug discovery/design resulting from the mutual interdependence of drug properties and behaviors (Figure 15).

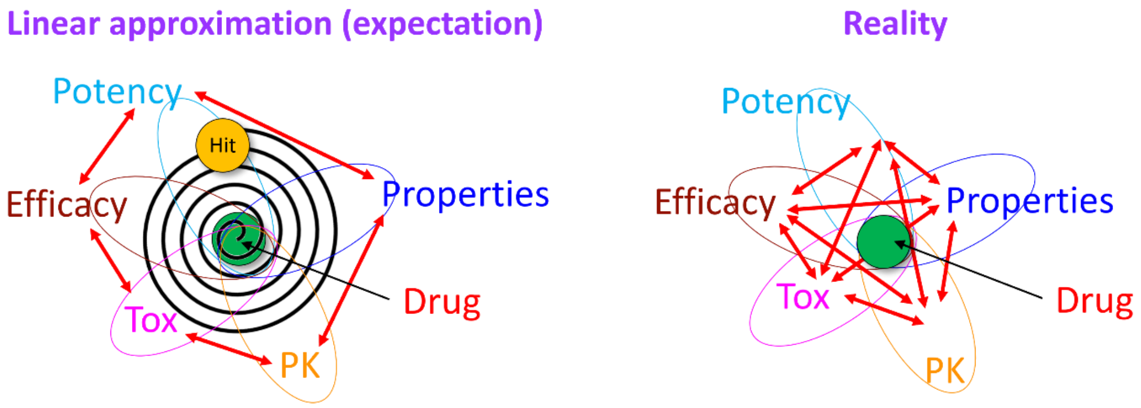

Figure 15. Left: a linear relationship among the major drug behaviors/properties is tacitly assumed under the status quo lead optimization paradigm. Predicted properties are optimized in a step-wise fashion, beginning with chemical starting points (hits) that "spiral" into predicted drugs via cycles of trial-and-error synthesis and testing. Right: in reality, such relationships are highly non-linear due to their mutual interdependence, such that optimization of one behavior may result in deoptimization of one or more others.

Based on our theory, lead optimization is ideally aimed at:

1) Minimizing the need for dose escalation during clinical testing (which erodes the safety margin and TI) by tuning k_{on} and k_{off} to the rates of target (or target binding site) buildup and decay, respectively,[2] such that the minimum efficacious γ_{eff} in humans is achieved at the lowest possible free C_{max}. Covalent reactions can be used to slow k_{off} when the amount of H-bond depleted solvation is insufficient to achieve the minimum efficacious γ_{eff} (noting that the covalent complexes of fluxes accumulate to their equilibrium levels over time).

2) Achieving the Goldilocks zone of solubility, permeability, and drug-target and drug-off-target binding, in which the overall desolvation costs are sufficiently low (reflected in higher logP). Optimal solvation properties correspond to:

   a) **The Goldilocks zone of solubility and desolvation costs incurred during drug-target and drug-membrane association** (Figure 16). Poorly soluble compounds dissolved in DMSO stock solutions (frequently used in assays) necessarily revert to their aqueous solubilization level and may distribute between solubilized (the bioavailable fraction), suspended, and precipitated fractions.

   b) Sufficient polar groups optimally positioned for low-cost desolvation of the polar phospholipid groups at membrane surfaces and target binding site regions solvated by H-bond enriched water (avoiding mismatches between non-polar drug groups and H-bond enriched solvation within the binding site).

   c) Sufficient non-polar groups optimally positioned for desolvating H-bond depleted regions of the target binding site (avoiding mismatches between polar drug groups and H-bond depleted solvation within the binding site).

   d) The gain of H-bond enriched solvation but not H-bond depleted or trapped/impeded solvation in the bound state (which respectively slows k_{off} and slows k_{on} and speeds k_{off}).

   e) **The lack of basic groups frequently used to solubilize poorly soluble compounds**. The solvation of such compounds is distributed asymmetrically between H-bond enriched solvation of the basic group and H-bond depleted solvation of the remaining scaffold (translating to amphipathicity/quasi-amphipathicity). Excess H-bond depleted relative to enriched solvation (the direct cause of poor solubility) can result in non-specific binding, membrane partitioning (i.e., high volume of distribution). Basic amines can further result in high levels of lysosomal trapping[27] and ion channel blockade.

f) The lowest possible molecular weight distributed between polar and non-polar groups required for matching H-bond enriched solvation on membrane and target binding site surfaces and depleted solvation on target binding site surfaces, respectively (the Goldilocks zone of chemical composition). This principle is captured in qualitative scalar form by the Lipinski rule of 5.[26]

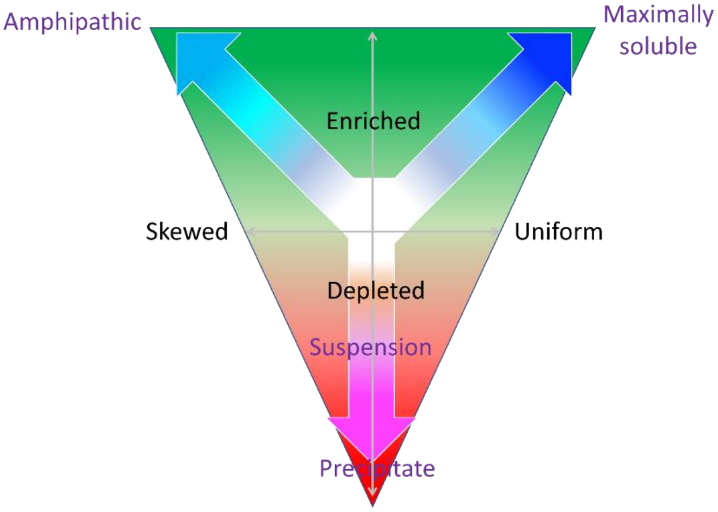

Figure 16. Maximal solubility depends on uniformly distributed H-bond enriched solvation across solute surfaces, which scales downward as the ratio of H-bond enriched/depleted solvation and absolute free energy magnitudes thereof decrease. The asymmetric distributions of H-bond enriched and depleted solvation in amphipathic molecules are exaggerated by acid groups and

basic amines. Precipitation occurs at a high threshold ratio of H-bond depleted to enriched solvation, whereas suspensions occur at a lower threshold ratio.

Activity cliffs (abrupt changes in potency due to small chemical changes) are due to significant k_{on} slowing, significant k_{off} speeding, or both. Slowed k_{on} relative to the reference analog is symptomatic of the loss of H-bond free energy among the partners due to:

1) Suboptimal H-bond replacement of H-bond enriched solvation of the modified analog and/or binding site relative to the reference analog, stemming from altered geometry and/or chemical composition of the offending R-group (translating to increased desolvation cost).

2) The generation of additional H-bond depleted solvation in the bound state of the modified analog compared with the reference, which destabilizes the bound state of the modified analog relative to the reference (translating to both slowed k_{on} and sped k_{off}).

Sped k_{off} is symptomatic of the loss of H-bond free energy among the partners (i.e., decreased resolvation cost) due to:

1) Reduced desolvation of H-bond depleted solvation of the modified analog and/or the binding site caused by spatial mismatching between the offending R-group and binding site relative to the reference.

2) The loss of additional H-bond enriched solvation generated in the bound state by the reference but not the modified analog, which destabilizes the bound state of the modified analog relative to the reference (manifesting as both slowed k_{on} and sped k_{off}).

Conclusion

Failure to achieve a TI during clinical testing in suitable patient populations stems from incorrectly predicted therapeutic effects of drug-target occupancy, structure-free energy relationships governing exposure-target occupancy (PK-PD) relationships, and/or overlapping minimum efficacious and toxic exposure levels in humans due in some cases to kinetically mistuned drug-target binding. ML and AI are generally useful for capturing weak signals in noisy datasets (e.g., protein sequence-tertiary/quaternary structure relationships in Alphafold2), but do not compensate for disconnects between dependent and independent variables (e.g., measured drug-target binding data and interatomic contact based molecular descriptors) and between disconnected contexts (e.g., equilibrium conditions in vitro versus non-equilibrium conditions in the native cellular setting). Predictions based on first principles theoretical understanding (the rules of the game) are far more likely to improve preclinical and clinical outcomes than empirical data models generated via ML, AI, or other means. Such models may help inspire, but not directly lead to first principles insights (e.g., quantum mechanics was not deduced from the Bohr atom; general relativity was not deduced from Newton's empirical gravitational principle). Biodynamics-guided drug design is concerned with the non-equilibrium solvation free energy contributions to solubility, permeability, kinetically tuned target binding kinetics, and kinetically mistuned off-target binding kinetics, which are necessarily optimized toward the Goldilocks zone <u>in parallel</u> (i.e., not too H-bond depleted and not too H-bond enriched) due to their non-linear relationship, in contrast to the status quo approach to drug discovery, in which these processes are optimized sequentially based on trial-and-error chemical synthesis guided by intuition/experience and empirical models derived from equilibrium data. Improving preclinical and clinical success rates depends to a large degree on shifting the paradigm from a trial-and-error, process-driven technology/chemistry-centric workflow to one guided by scientific principles that are better aligned with the native cellular setting.

References

1. Wong, C. H., Siah, K. W. & Lo, A. W. Estimation of clinical trial success rates and related parameters. *Biostatistics* **20**, 273–286 (2019).
2. Selvaggio, G. & Pearlstein, R. A. Biodynamics: A novel quasi-first principles theory on the fundamental mechanisms of cellular function/dysfunction and the pharmacological modulation thereof. *PLoS One* **13**, e0202376 (2018).
3. Pearlstein, R. A. *et al.* Building New Bridges between In Vitro and In Vivo in Early Drug Discovery: Where Molecular Modeling Meets Systems Biology. *Curr. Top. Med. Chem.* **17**, 1–1 (2017).
4. Pearlstein, R. A., Wan, H. & Aravamuthan, V. Toward in vivo relevant drug design. *Drug Discov. Today* **26**, 637–650 (2021).
5. Wan, H., Aravamuthan, V. & Pearlstein, R. A. Probing the Dynamic Structure-Function and Structure-Free Energy Relationships of the Coronavirus Main Protease with Biodynamics Theory. *ACS Pharmacol. Transl. Sci.* **3**, 1111–1143 (2020).
6. Selvaggio, G., Wan, H. & Pearlstein, R. A. Probing cellular arrhythmogenesis using the O'Hara-Rudy model of the undiseased human ventricular cardiomyocyte. *bioRxiv* 2020.11.15.384032 (2020) doi:10.1101/2020.11.15.384032.
7. Wan, H. *et al.* Solvation dynamics-powered structure and function of multi-molecular cellular systems exemplified by non-equilibrium cereblon-degrader-CK1α ternary complex formation. *bioRxiv* 2021.10.29.466510 (2021) doi:10.1101/2021.10.29.466510.
8. Wan, H. & Pearlstein, R. A. Toward a first principles understanding of the activation and deactivation mechanisms of class A G-protein coupled receptors and voltage-gated cation channels. doi:10.1101/2022.03.29.486149.

9. Wan, H., Selvaggio, G. & Pearlstein, R. Toward in vivo -relevant hERG safety assessment and mitigation strategies based on relationships between non-equilibrium blocker binding, three-dimensional channel-blocker interactions, dynamic occupancy, dynamic exposure, and cellular arrhythmia. *PLoS One* **15**, e0234946 (2020).

10. Wan, H., Spiru, K., Williams, S. & Pearlstein, R. A. General structure-free energy relationships of hERG blocker binding under native cellular conditions. *bioRxiv* (2021) doi:10.1101/2021.10.07.463585.

11. Noble, D. *The Music of Life: Biology Beyond the Genome*. (Oxford University Press, 2006).

12. Tran, Q.-T. *et al.* Structure-kinetic relationship of carbapenem antibacterials permeating through E. coli OmpC porin. *Proteins Struct. Funct. Bioinforma.* **82**, (2014).

13. Tran, Q. T., Williams, S., Farid, R., Erdemli, G. & Pearlstein, R. The translocation kinetics of antibiotics through porin OmpC: Insights from structure-based solvation mapping using WaterMap. *Proteins Struct. Funct. Bioinforma.* **81**, 291–299 (2013).

14. Pearlstein, R. A. *et al.* New hypotheses about the structure-function of proprotein convertase subtilisin/kexin type 9: Analysis of the epidermal growth factor-like repeat A docking site using watermap. *Proteins Struct. Funct. Bioinforma.* **78**, 2571–2586 (2010).

15. Pearlstein, R. A., Sherman, W. & Abel, R. Contributions of water transfer energy to protein-ligand association and dissociation barriers: Watermap analysis of a series of p38α MAP kinase inhibitors. *Proteins Struct. Funct. Bioinforma.* **81**, (2013).

16. Velez-Vega, C., McKay, D. J. J., Aravamuthan, V., Pearlstein, R. & Duca, J. S. Time-averaged distributions of solute and solvent motions: Exploring proton wires of GFP and PfM2DH. *J. Chem. Inf. Model.* **54**, (2014).

17. Kneller, D. W. *et al.* Covalent narlaprevir- and boceprevir-derived hybrid inhibitors of SARS-CoV-2 main protease. *Nat. Commun.* **13**, (2022).

18. Boras, B. *et al.* Discovery of a Novel Inhibitor of Coronavirus 3CL Protease as a Clinical Candidate for the Potential Treatment of COVID-19. *bioRxiv* 2020.09.12.293498 (2020) doi:10.1101/2020.09.12.293498.

19. Case, D. A. *et al.* Amber 2022.

20. Case, D. A. *et al.* The Amber biomolecular simulation programs. *Journal of Computational Chemistry* vol. 26 1668–1688 (2005).

21. Shi, J., Sivaraman, J. & Song, J. Mechanism for Controlling the Dimer-Monomer Switch and Coupling Dimerization to Catalysis of the Severe Acute Respiratory Syndrome Coronavirus 3C-Like Protease. *J. Virol.* **82**, 4620–4629 (2008).

22. Velez-Vega, C. *et al.* Estimation of solvation entropy and enthalpy via analysis of water oxygen-hydrogen correlations. *J. Chem. Theory Comput.* **11**, (2015).

23. Owen, D. R. *et al.* An oral SARS-CoV-2 Mpro inhibitor clinical candidate for the treatment of COVID-19. *Science (80-.).* **374**, 1586–1593 (2021).

24. Merlot, A. M., Kalinowski, D. S. & Richardson, D. R. Unraveling the mysteries of serum albumin-more than just a serum protein. *Front. Physiol.* **5 AUG**, 299 (2014).

25. Young, T., Abel, R., Kim, B., Berne, B. J. & Friesner, R. A. Motifs for molecular recognition exploiting hydrophobic enclosure in protein-ligand binding. *Proc. Natl. Acad. Sci. U. S. A.* **104**, 808–813 (2007).

26. Lipinski, C. A. Drug-like properties and the causes of poor solubility and poor permeability. *J. Pharmacol. Toxicol. Methods* **44**, 235–249 (2000).

27. Llanos, S. *et al.* Lysosomal trapping of palbociclib and its functional implications.

Oncogene **38**, 3886–3902 (2019).